Geological Magazine

www.cambridge.org/geo

Original Article

Cite this article: Li R-W, Zhang X, Shi Q, Chen W-F, An Y, Huang Y-S, Liu Y-X, and Wang J-R (2020) Early Permian to Late Triassic tectonics of the southern Central Asian Orogenic Belt: geochronological and geochemical constraints from gabbros and granites in the northern Alxa area, NW China. *Geological Magazine* **157**: 2089–2105. https://doi.org/10.1017/S0016756820000345

Received: 5 September 2019
Revised: 4 March 2020
Accepted: 30 March 2020
First published online: 27 April 2020

Keywords:
Alxa area; Central Asian Orogenic Belt; gabbros and granites; tectonics; late Permian to Early–Middle Triassic

Author for correspondence:
Jin-Rong Wang, Email: jrwang@lzu.edu.cn

Early Permian to Late Triassic tectonics of the southern Central Asian Orogenic Belt: geochronological and geochemical constraints from gabbros and granites in the northern Alxa area, NW China

Run-Wu Li[1], Xin Zhang[2], Qiang Shi[1], Wan-Feng Chen[1], Yi An[3], Yao-Shen Huang[1], Yi-Xin Liu[1] and Jin-Rong Wang[1]

[1]School of Earth Sciences and Gansu Key Laboratory of Mineral Resources in Western China, Lanzhou University, Lanzhou 730000, PR China; [2]College of Resources & Environmental Science, Ningxia University, Yinchuan 750021, PR China and [3]Guangzhou Institute of Geochemistry, Chinese Academy of Sciences, Guangzhou 510640, PR China

Abstract

Situated between the North China Craton to the east and the Tarim Craton to the west, the northern Alxa area in westernmost Inner Mongolia in China occupies a key location for interpreting the late-stage tectonic evolution of the southern Central Asian Orogenic Belt. New LA-ICP-MS zircon U–Pb dating results reveal 282.2 ± 3.9 Ma gabbros and 216.3 ± 3.2 Ma granites from the Yagan metamorphic core complex in northern Alxa, NW China. The gabbros are characterized by low contents of Si, Na, K, Ti and P and high contents of Mg, Ca, Al and Fe. These gabbros have arc geochemical signatures with relative enrichments in large ion lithophile elements and depletions in high field strength elements, as well as negative εNd(t) (−0.91 to −0.54) and positive εHf(t) (2.59 to 6.37) values. These features indicate that a depleted mantle magma source metasomatized by subduction fluids/melts and contaminated by crustal materials was involved in the processes of magma migration and emplacement. The granites show high-K calc-alkaline and metaluminous to weakly peraluminous affinities, similar to A-type granites. They have positive εNd(t) (1.55 to 1.99) and εHf(t) (5.03 to 7.64) values. These features suggest that the granites were derived from the mixing of mantle and crustal sources and formed in a postcollisional tectonic setting. Considering previous studies, we infer that the final closure of the Palaeo-Asian Ocean in the central part of the southern Central Asian Orogenic Belt occurred in late Permian to Early–Middle Triassic times.

1. Introduction

The closure of the long-lived Palaeo-Asian Ocean (PAO) generated the Central Asian Orogenic Belt (CAOB), which is situated between the North China and Tarim cratons to the south, Siberian Craton to the north and Baltica Craton to the west (Fig. 1a). The CAOB mainly consists of microcontinents, island arcs, ophiolitic remnants and ocean plate stratigraphy (Wan *et al.* 2018), is famous as the world's largest accretionary orogenic belt and represents a major site of significant Phanerozoic continental growth (Sengör *et al.* 1993; Jahn *et al.* 2000; Badarch *et al.* 2002; Xiao *et al.* 2004, 2009, 2015, 2019). Some authors also call the CAOB the Altaids (Sengör *et al.* 1993; Windley *et al.* 2007). In past decades, many studies have been carried out, focusing on the closure of the ocean, the consequent architecture of the orogenic belt and the related continental growth (Zuo *et al.* 1990; Wang *et al.* 1993, 1994; Wu & He, 1993; Wu *et al.* 1998; Xiao *et al.* 2003, 2004, 2009; Charvet *et al.* 2011; Xu *et al.* 2013; Liu *et al.* 2016, 2017, 2018; Fei *et al.* 2019). The PAO is widely accepted to have finally closed along the northern margins of the North China and Tarim cratons (Sengör *et al.* 1993; Xiao *et al.* 2015, 2019). However, because of the different research methods used by different authors and the complex processes of accretionary orogenesis in the CAOB, the timing of the final closure of the PAO is still under debate, with a wide time span ranging from the Late Devonian to the Triassic (Xiao *et al.* 2009; Han *et al.* 2010; Charvet *et al.* 2011; Xu *et al.* 2013; Liu *et al.* 2016, 2017).

The northern Alxa area in westernmost Inner Mongolia in China is situated in the central part of the southern CAOB, which is a key location connecting the North China Craton to the east and the Tarim Craton to the west. However, much less attention has been paid to this area, hampering the achievement of a better understanding of the final closure process of the PAO in this part of the southern CAOB. The study region in the northern Alxa area is part of the Yagan metamorphic core complex (Yagan MCC) (Zheng *et al.* 1991; Zheng & Zhang, 1994;

https://doi.org/10.1017/S0016756820000345 Published online by Cambridge University Press

Webb *et al.* 1999). Previous studies inferred that the final closure of the PAO in this area took place during a span from the late Permian to Middle Triassic period according to sedimentary records in the area of the Yagan MCC, but this conclusion has not been well supported by geochronological and geochemical evidence from magmatic rocks (Zheng & Zhang, 1994). Late Palaeozoic to Mesozoic magmatic rocks are widespread in the area of the Yagan MCC, mainly including Palaeozoic gabbros and Mesozoic granitic rocks (Fig. 2; Wang & Zheng, 2002; Wang *et al.* 2004; Feng *et al.* 2013), which can provide constraints on the evolutionary history of the central part of the southern CAOB and help us better understand the closure process of the PAO. However, only a mylonitic potassic granitic pluton with an isotopic age of 228 Ma, which experienced syn-emplacement extensional deformation (Wang *et al.* 2002), has been studied in detail, and the Palaeozoic gabbros have not been well studied at all. Therefore, in this study, we present new zircon U–Pb dating results, whole-rock major- and trace-element data and Nd–Hf isotope data for the Palaeozoic gabbros and the Mesozoic granites in the Yagan MCC area. These new data, combined with regional geological data, can provide constraints on the conditions and tectonic settings of magma production and thus constrain the timing of the final closure of the PAO.

2. Geological background

The Alxa area is located in western Inner Mongolia and separated from the early Palaeozoic North Qilian Orogenic Belt by the Longshoushan Fault to the south and from the North China Craton by the Langshan Fault to the east (Song *et al.* 2018). Three major fault belts have been recognized in the Alxa area, which are termed, from north to south, the Yagan Fault Belt, the Enger Us Fault Belt and the Quagan Qulu Fault Belt (also called the Badain Jaran Fault) (Wu & He, 1993). The Yagan Fault Belt has been suggested to represent an important boundary according to the comparable lithology of the southern and northern flanks of the boundary (Zhang *et al.* 2017; Liu *et al.* 2018). An ophiolitic mélange belt is exposed along the Enger Us Fault Belt, which is generally regarded as a major suture zone separating the CAOB to the north from the North China Craton to the south (Wang *et al.* 1994). An ophiolitic mélange belt also occurs along the Quagan Qulu Fault Belt, which is considered to represent remnants of a back-arc basin that formed as a result of the southward subduction of the Enger Us Ocean (Zheng *et al.* 2014). All three faults divide the Alxa area into four major tectonic zones from north to south: the Yagan tectonic zone (YTZ), the Zhusileng–Hangwula tectonic zone (ZHTZ), the Zongnaishan–Shalazhashan tectonic zone (ZSTZ) and the Nuru–Langshan tectonic zone (NLTZ) (Fig. 1b).

The Yagan MCC, which is located in the northern ZHTZ, consists of an upper plate, a lower plate and a master detachment fault (Fig. 2). The upper plate mainly includes Permian, Triassic, Jurassic and Lower Cretaceous rocks. Regionally, the upper Permian rocks experienced folding and lower greenschist-facies metamorphism, while the Upper Triassic rocks are characterized by terrestrial redbeds and conglomerates and did not experience regional metamorphism, which implies that the final closure of the PAO in this area took place in late Permian to Middle Triassic times (Zheng & Zhang, 1994; Wang *et al.* 2002). The study area, which is situated next to the Jindouaobao area, is part of the lower plate of the Yagan MCC. The stratigraphic sequence of the lower plate is mainly Precambrian amphibolite-facies metamorphic rocks. The magmatic rocks distributed in the region mostly consist of Mesozoic granitic plutons, with very few Palaeozoic gabbro intrusive bodies. Between the two plates is the master detachment fault (Wang *et al.* 2004). In the field, a series of normal faults has developed in the study region and has been considered a result of the extensional deformation of the crust in this area (Fig. 2; Zheng & Zhang, 1994; Wang & Zheng, 2002; Wang *et al.* 2002). The early Mesozoic granitic plutons intrude the Precambrian metamorphic rocks along normal faults. They have been strongly deformed, presenting a linear-shaped texture parallel to the regional extensional shear foliation. The gabbros scattered within the studied area have also been strongly deformed, showing orientation of plagioclase and clinopyroxene to some extent. They formed dykes, and the contact relationships with the country rocks are not visible in the field. Most of the dykes are cut by normal faults, which implies that the gabbro plutons formed before the normal faults (Fig. 2).

3. Samples and analytical methods

3.a. Description of samples

To achieve precise geochemical and geochronological results, in this study, fresh gabbro and granite samples from the Yagan MCC area in the north of the ZHTZ were collected. Field photographs of the gabbro and granite samples are shown in Figure 3a and Figure 3b, respectively. Detailed sampling locations are shown in Figure 2.

3.a.1. Gabbro

Six gabbro samples (16YG-62 to 67) were collected from the core of a 750×3000 m^2 intrusive body (Fig. 2). The gabbro samples have been strongly deformed, showing orientation of plagioclase and clinopyroxene to some extent, and should be called microgabbro. They are black in colour and fine- to medium-grained rocks. The major minerals are plagioclase (± 45 %) and clinopyroxene (± 50 %), with very few olivine grains (± 5 %). Plagioclase is subhedral and has been altered. Clinopyroxene and olivine are euhedral compared to plagioclase and have also been altered to some extent (Fig. 3c, d).

3.a.2. Granites

Six granite samples (16YG-55 to 60) were collected from the core of a 1000×1750 m^2 intrusion (Fig. 2). The samples have been strongly deformed, presenting a gneissic structure. They show foliation and stretching lineations defined by compositional banding of both K-feldspar and quartz crystals parallel to the regional extensional shear. The samples comprise mainly quartz (± 60 %), plagioclase (± 25 %), K-feldspar (± 10 %) and biotite (± 5 %). Quartz crystals usually present undulatory extinction due to ductile shear deformation. Biotite grains are irregular owing to secondary alteration and display preferred orientations (Fig. 3e, f).

3.b. Analytical methods

3.b.1. Major- and trace-element analyses

Analyses of major and trace elements were carried out at the Key Laboratory of Mineral Resources in Western China, School of Earth Sciences, Lanzhou University. Major elements were determined by inductively coupled plasma optical emission spectroscopy (ICP-OES) using a Leeman Prodigy system with an analytical precision greater than 2 %. Loss on ignition (LOI) was obtained by heating approximately 0.5 g of dried sample powder at 1000 °C for 2 hours. Trace elements were determined by inductively coupled plasma mass spectrometry (ICP-MS) with an Agilent 7700X instrument that was used to analyse solutions

https://doi.org/10.1017/S0016756820000345 Published online by Cambridge University Press

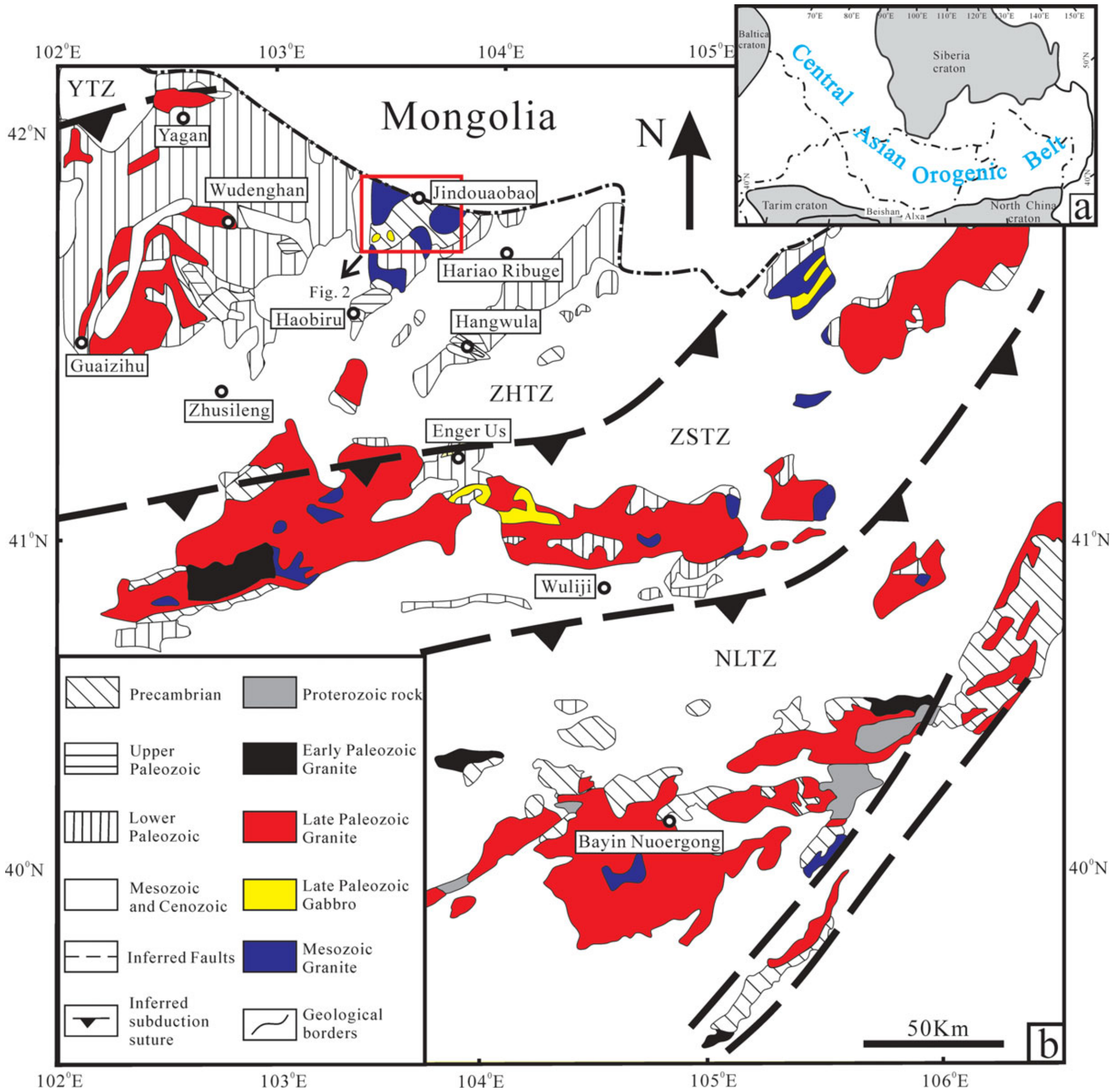

Fig. 1. (Colour online) (a) Geological map of the Central Asian Orogenic Belt (modified after Jahn *et al*. 2000). (b) Geological map of the Alxa area (modified after Feng *et al*. 2013). Four tectonic zones from north to south: YTZ – Yagan tectonic zone; ZHTZ – Zhusileng–Hangwula tectonic zone; ZSTZ – Zongnaishan–Shalazhashan tectonic zone; NLTZ – Nuru–Langshan tectonic zone.

of the samples digested by HF + $HClO_4$ acid in bombs. The US Geological Survey rock reference materials AGV-2 and BCR-2 were used for quality control. The relative standard deviation was less than 10 % for the determination of trace elements, including rare earth elements (REEs).

3.b.2. Zircon U–Pb dating

Separation of zircon crystals was completed using conventional heavy liquid and magnetic techniques, and these zircon grains were then mounted in epoxy resin and polished to approximately half thickness at Langfang Chenxin Geological Service Co., Hebei, China. Zircon grains presenting clear and less fractured rims in cathodoluminescence (CL) images were chosen as suitable targets for U–Pb dating. The U–Pb isotope ratios of selected zircons were measured using an Agilent 7500X ICP-MS instrument combined with a Geo-Las200M laser ablation (LA) system at the Key Laboratory of Mineral Resources in Western China, School of Earth Sciences, Lanzhou University. Zircon standard 91500 (Wiedenbeck *et al.* 1995) was used as the age standard. Reference glass NIST 610 (Pearce *et al.* 1997) and ^{29}Si were applied as external and internal standards, respectively, during the process of analysing zircon element compositions. The spot diameter was ~30 μm. Data reduction was performed using the Glitter (ver. 4.0) program, and common Pb was corrected using the Common Lead correction (ver. 3.15) program (Andersen, 2002). Concordia plots were created and weighted mean ages calculated using the Isoplot (ver. 3.0) program (Ludwig, 2003).

3.b.3. Whole-rock Sm–Nd and Lu–Hf isotopes

Whole-rock Sm–Nd and Lu–Hf isotope compositions were determined by a Nu Plasma II multi-collector (MC)-ICP-MS (Nu Instruments, UK) at the Key Laboratory of Mineral Resources in Western China, School of Earth Sciences, Lanzhou University. The US Geological Survey rock reference

https://doi.org/10.1017/S0016756820000345 Published online by Cambridge University Press

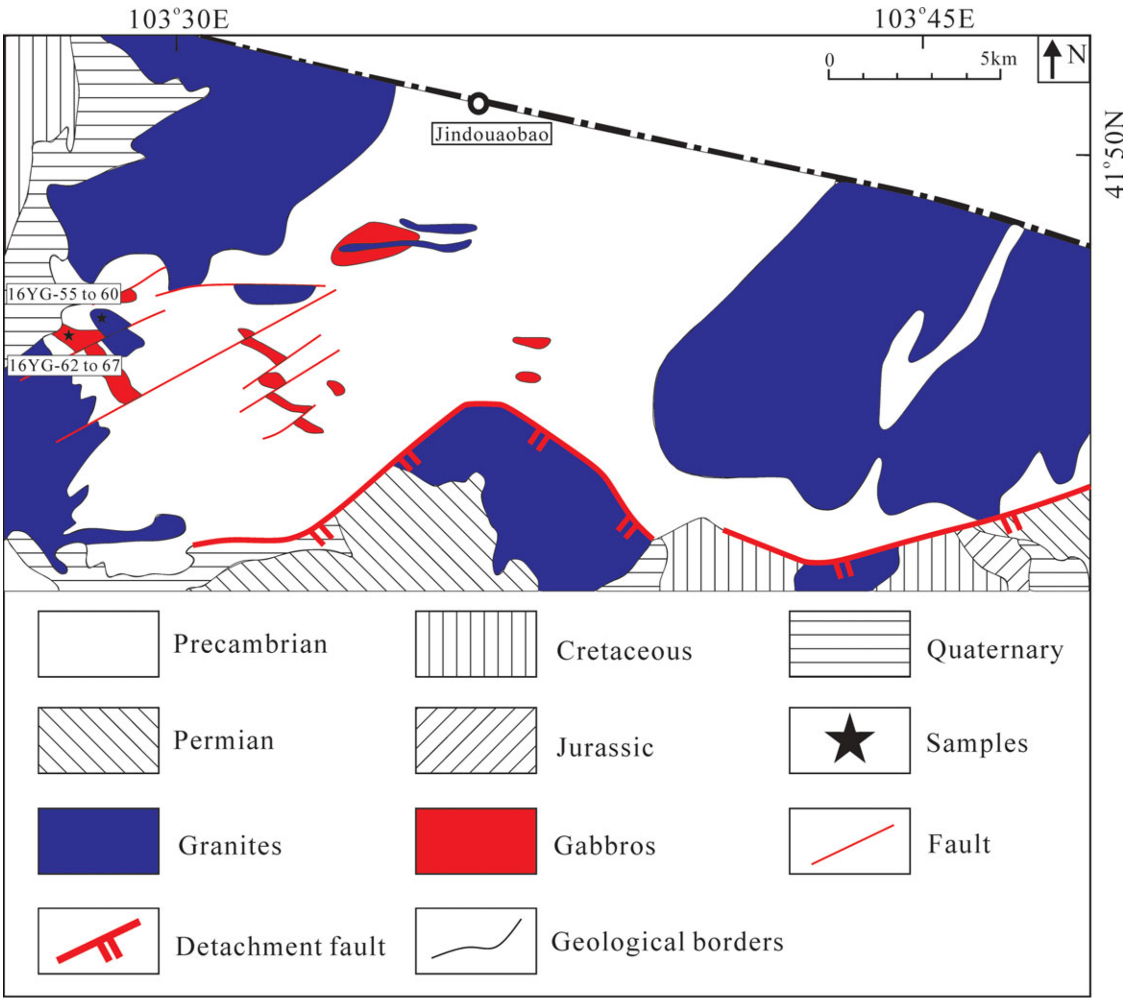

Fig. 2. (Colour online) Geological map of the studied area (modified after BGNHAR, 1982).

materials AGV-2 and BCR-2 were used as standard samples. During the process of measurement, JNDI and Alfa Hf standard solution were used for quality control of Nd and Hf, respectively.

4. Results

4.a. Major-element geochemistry

4.a.1. The gabbros

The major-element concentrations of the gabbros are presented in Table 1. The gabbros exhibit low contents of SiO_2 (48.88–51.15 wt %), Na_2O (1.15–2.47 wt %), K_2O (0.42–0.67 wt %), TiO_2 (0.36–0.55 wt %) and P_2O_5 (0.06–0.13 wt %) and high contents of CaO (11.87–13.77 wt %), Al_2O_3 (14.98–17.10 wt %) and total Fe_2O_3 (6.86–7.74 wt %). The Mg numbers ($100*(Mg^{2+}/(Mg^{2+}+Fe^{2+}))$, 68–69) are relatively high. All gabbro samples plot in the gabbro field on the ($Na_2O + K_2O$) versus SiO_2 diagram (Fig. 4). They all belong to the metaluminous series (Fig. 5b, d) and present enrichments in Mg and Fe (Fig. 5a).

4.a.2. The granites

The major-element concentrations of the granites are presented in Table 1. The granites in this area show high concentrations of SiO_2 (75.19–78.14 wt %) and low concentrations of total Fe_2O_3 (0.94–1.12 wt %), CaO (0.60–0.96 wt %), TiO_2 (0.08–0.18 wt %) and P_2O_5 (0.01–0.06 wt %). The total alkali ($Na_2O + K_2O$) and Al_2O_3 concentrations are 7.70–8.80 wt % and 11.11–12.74 wt %, respectively. These samples plot in the granite field on the ($Na_2O + K_2O$) versus SiO_2 diagram (Fig. 4), displaying high-K calc-alkaline (Fig. 5c) and metaluminous to weakly peraluminous affinities with moderate A/CNK (molar ratio of $Al_2O_3/(Na_2O + K_2O + CaO)$) values of 0.78 to 0.90 (Fig. 5b, d).

4.b. Trace-element geochemistry

4.b.1. The gabbros

The trace-element concentrations of the gabbros are shown in Table 1. As shown in the chondrite-normalized REE diagram (Fig. 6a), the gabbros from the region have low REE contents (34.51–51.15 ppm), displaying light REE (LREE) enrichment relative to heavy REEs (HREEs) (LREE/HREE = 3.58–4.32, $(La/Yb)_N = 3.23–4.32$, $(La/Sm)_N = 1.91–2.44$). These features are similar to those of enriched mid-ocean ridge basalt (E-MORB). In addition, the samples show negative Eu anomalies ($\delta Eu = 0.76–0.96$), which can be attributed to the fractional crystallization of feldspar during the magmatic process. On the primitive mantle-normalized spider diagram (Fig. 6b), all samples present

https://doi.org/10.1017/S0016756820000345 Published online by Cambridge University Press

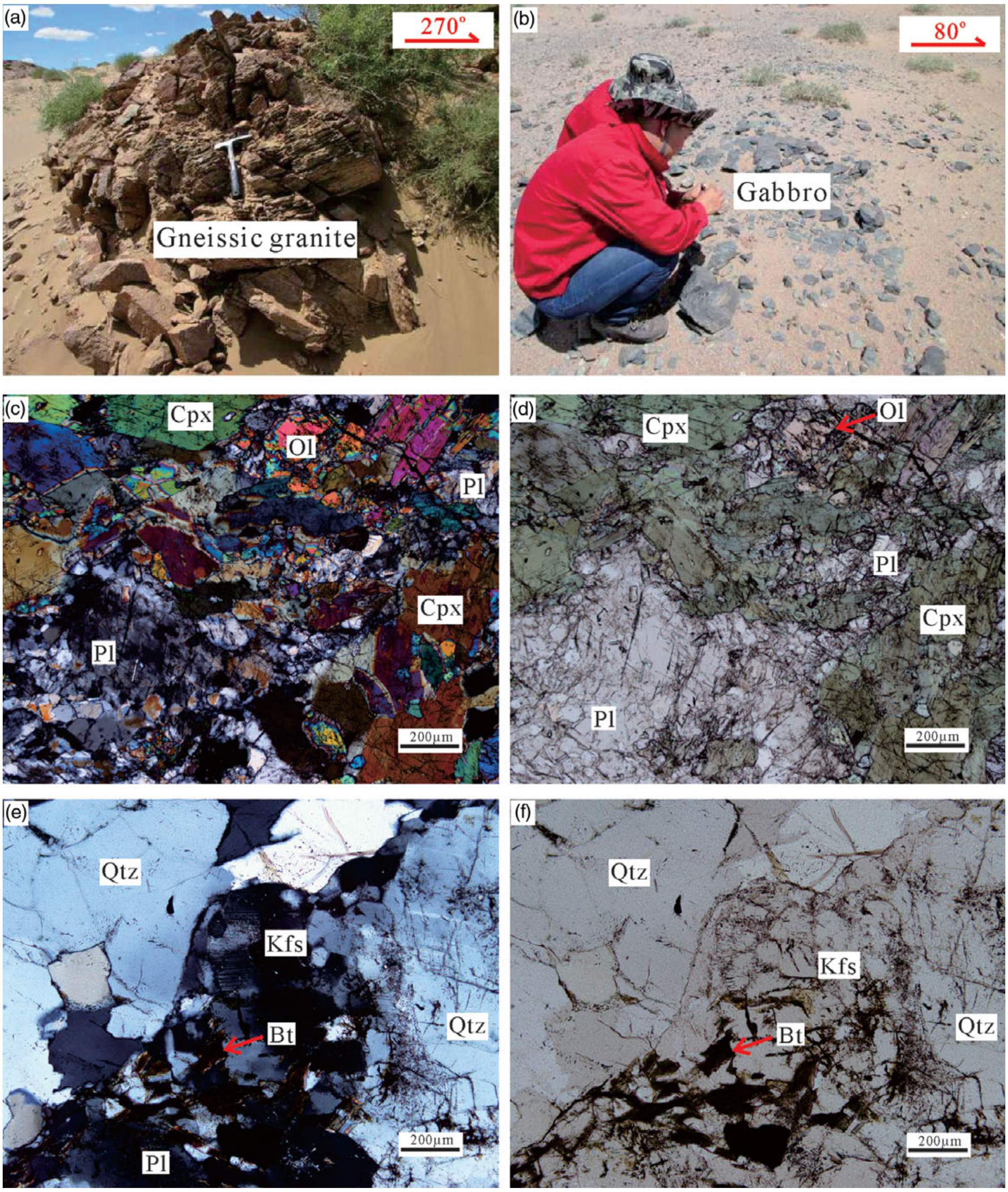

Fig. 3. (Colour online) Field photographs and microphotographs of the gabbros and granites in the area of the Yagan MCC. (a) Field photographs of granitic rocks. Length of hammer for scale is ~30 cm. (b) Field photographs of gabbroic rocks. (c) Cross-polarized photograph of the gabbro sample 16YG-64. (d) Plane-polarized photograph of the gabbro sample 16YG-64. (e) Cross-polarized photograph of the granite sample 16YG-55. (f) Plane-polarized photograph of the granite sample 16YG-55. Abbreviations: Ol – olivine; Cpx – clinopyroxene; Pl – plagioclase; Qtz – quartz; Kfs – K-feldspar; Bt – biotite.

clear enrichments in large ion lithophile elements (LILEs; e.g. Rb, Ba, Sr, Pb and U) and depletions in Nb and Ta without evident Ti depletion.

4.b.2. The granites

The trace-element concentrations of the granites are shown in Table 1. On the chondrite-normalized REE diagram (Fig. 6c) all granites show strong LREE enrichments compared to HREEs ($(La/Yb)_N = 7.67–82.79$). Four granite samples have negative Eu anomalies ($\delta Eu = 0.48–0.73$), interpreted as resulting from the fractional crystallization of feldspar. They are all enriched in LILEs and depleted in high field strength elements (HFSEs; Nb, Ta and Ti) (Fig. 6d).

4.c. Zircon U–Pb ages

4.c.1. The gabbros

The U–Pb isotope analytical results for the zircons from a gabbro sample (16YG-66) are listed in Table 2. The dated sample weighed 20 kg, and ~300 zircon crystals were separated from the gabbro. Then, 25 zircon crystals from the gabbro sample were selected as suitable targets for U–Pb dating. They are generally euhedral with short columnar shapes. In the CL images (Fig. 7a), they

https://doi.org/10.1017/S0016756820000345 Published online by Cambridge University Press

Table 1. Major- and trace-element compositions (in ppm) and parameters of the granites and the gabbros in the Yagan MCC area

Sample number	YG-55	YG-56	YG-57	YG-58	YG-59	YG-60	YG-62	YG-63	YG-64	YG-65	YG-66	YG-67
Lithology	Granite	Granite	Granite	Granite	Granite	Granite	Gabbro	Gabbro	Gabbro	Gabbro	Gabbro	Gabbro
SiO_2	76.77	76.49	75.19	78.14	77.59	77.12	50.25	49.87	49.42	49.79	48.88	51.15
TiO_2	0.14	0.08	0.10	0.14	0.18	0.16	0.44	0.36	0.55	0.54	0.44	0.50
Al_2O_3	11.36	12.03	12.74	11.50	11.93	11.11	16.36	17.10	15.28	14.98	15.30	15.01
TFe_2O_3	1.04	0.94	1.05	0.94	1.11	1.12	7.12	6.86	7.70	7.34	7.61	7.74
MnO	0.01	0.01	0.03	0.01	0.02	0.01	0.11	0.12	0.13	0.12	0.13	0.13
MgO	0.13	0.08	0.08	0.15	0.14	0.15	8.78	8.28	9.70	9.31	9.36	9.15
CaO	0.66	0.96	0.90	0.91	0.75	0.60	12.43	11.87	13.10	13.77	12.87	12.50
Na_2O	2.92	3.30	3.71	2.78	2.81	2.98	2.36	2.47	1.91	1.15	2.01	1.78
K_2O	5.59	5.19	5.19	4.92	5.50	5.87	0.61	0.51	0.43	0.42	0.64	0.67
P_2O_5	0.01	0.02	0.01	0.02	0.01	0.06	0.13	0.07	0.11	0.06	0.06	0.12
LOI	0.28	0.30	0.81	0.43	0.27	0.39	1.17	1.81	1.35	1.26	1.20	1.22
Total	98.92	99.40	99.83	99.94	100.30	99.58	99.75	99.30	99.69	98.74	98.50	99.97
Mg no.	19	13	12	22	18	19	69	68	69	69	69	68
A/CNK	0.83	0.85	0.87	0.90	0.88	0.78	0.78	0.84	0.73	0.72	0.72	0.73
Ba	207	23.69	28.69	221	420	207	1945	161	273	981	142	160
Rb	114	209	154	110	215	123	19.24	21.99	10.20	13.01	33.46	38.16
Cs	1.25	12.07	9.17	2.18	14.95	1.02	1.74	8.60	1.16	2.12	1.34	1.61
Th	12.85	1.26	3.13	6.70	15.07	14.69	9.08	3.08	2.25	2.17	1.92	1.49
U	0.58	0.49	0.70	0.87	0.71	0.67	1.38	0.62	0.97	0.81	0.57	0.57
Nb	9.37	3.52	7.49	5.90	6.58	6.17	2.09	1.57	2.28	3.91	2.06	2.28
Ta	0.38	0.12	0.18	0.21	0.85	0.16	0.16	0.10	0.15	0.22	0.14	0.14
K	46427	43114	43104	40824	45618	48718	5045	4210	3609	3523	5342	5585
Pb	20.65	22.69	25.62	21.70	26.64	21.59	6.78	7.53	7.10	4.93	5.74	5.23
Sr	61.17	17.34	12.78	70.88	96.99	64.03	475	460	427	606	340	356
Zr	31.25	12.65	41.78	105	56.51	100	27.37	41.55	48.50	67.45	27.13	46.43
Hf	1.00	0.52	1.73	3.83	1.83	3.39	1.13	1.32	1.61	2.26	1.16	1.73
P	43.65	65.73	42.39	69.20	43.65	277	578	285	489	246	284	518
Ti	864	487	588	854	1080	947	2611	2143	3295	3222	2614	2976
Cr	3.74	4.06	1.52	0.73	2.40	5.52	267	258	563	630	576	594
Ni	2.40	2.01	1.01	0.50	2.08	3.39	76.94	65.71	84.10	83.72	82.30	83.50
Co	0.99	0.26	0.18	0.89	1.12	128	29.69	29.33	31.61	32.51	30.89	39.91
V	7.41	1.95	0.61	6.44	14.85	9.92	105	101	133	157	126	135
Sc	1.49	5.94	2.41	1.92	1.65	2.09	26.54	28.09	33.39	35.32	32.34	33.53
Ga	21.02	16.34	17.18	15.69	20.41	20.69	13.21	14.39	13.49	13.10	12.99	14.03
La	62.94	4.24	6.12	23.57	48.65	56.89	7.05	5.79	6.84	9.06	7.19	6.94
Ce	131	5.75	9.04	34.26	89.70	132	12.53	10.38	12.89	16.39	12.43	12.68
Pr	14.88	1.09	1.67	5.01	10.21	13.96	1.91	1.67	2.11	2.57	1.93	2.04
Nd	52.71	4.80	6.71	18.18	34.82	49.25	8.11	7.13	9.45	10.51	8.20	8.77
Sm	7.90	1.55	1.63	3.16	4.24	7.02	1.96	1.73	2.32	2.40	1.91	2.15
Eu	1.04	0.29	0.37	1.23	1.14	0.98	0.57	0.56	0.68	0.62	0.60	0.64
Gd	4.89	1.46	1.41	2.18	2.25	4.01	2.03	1.86	2.44	2.52	2.05	2.31
Tb	0.66	0.21	0.19	0.28	0.22	0.43	0.32	0.32	0.41	0.41	0.34	0.37

(*Continued*)

https://doi.org/10.1017/S0016756820000345 Published online by Cambridge University Press

Table 1. (*Continued*)

Sample number	YG-55	YG-56	YG-57	YG-58	YG-59	YG-60	YG-62	YG-63	YG-64	YG-65	YG-66	YG-67
Lithology	Granite	Granite	Granite	Granite	Granite	Granite	Gabbro	Gabbro	Gabbro	Gabbro	Gabbro	Gabbro
Dy	3.62	1.12	0.96	1.37	1.00	2.07	2.12	1.94	2.61	2.61	2.17	2.34
Ho	0.64	0.18	0.16	0.25	0.17	0.34	0.43	0.41	0.55	0.54	0.45	0.49
Er	1.67	0.51	0.41	0.68	0.45	0.87	1.30	1.22	1.60	1.58	1.32	1.46
Tm	0.20	0.06	0.06	0.10	0.05	0.11	0.18	0.17	0.23	0.23	0.19	0.20
Yb	1.16	0.40	0.39	0.67	0.42	0.65	1.26	1.15	1.52	1.50	1.30	1.39
Lu	0.14	0.05	0.06	0.12	0.06	0.11	0.20	0.17	0.23	0.22	0.19	0.20
Y	14.72	4.81	4.63	5.95	4.59	7.89	11.25	10.45	14.12	13.95	11.64	12.72
ΣREE	283.80	21.71	29.17	91.05	193.39	268.45	39.99	34.51	43.88	51.15	40.26	41.99
LREE	270.82	17.73	25.54	85.42	188.76	259.86	32.14	27.27	34.29	41.54	32.25	33.22
HREE	12.98	3.99	3.64	5.63	4.63	8.59	7.85	7.24	9.59	9.61	8.01	8.77
LREE/HREE	20.86	4.44	7.02	15.17	40.78	30.25	4.10	3.77	3.58	4.32	4.03	3.79
δEu	0.48	0.59	0.73	1.36	1.01	0.52	0.87	0.96	0.87	0.76	0.93	0.87
δCe	1.02	0.64	0.68	0.74	0.94	1.11	0.82	0.81	0.83	0.82	0.80	0.82
$(La/Yb)_N$	38.86	7.67	11.26	25.38	82.79	62.48	4.00	3.61	3.23	4.32	3.98	3.57
$(Gd/Yb)_N$	3.48	3.04	2.99	2.70	4.42	5.08	1.33	1.34	1.33	1.39	1.31	1.37
$(La/Sm)_N$	5.15	1.77	2.43	4.81	7.40	5.23	2.32	2.16	1.91	2.44	2.43	2.08

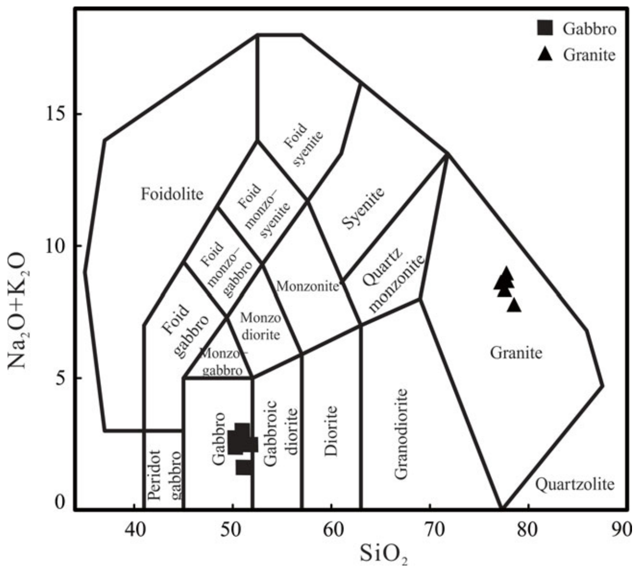

Fig. 4. Total alkali ($Na_2O + K_2O$) versus silica (SiO_2) diagram (Middlemost, 1994).

exhibit obvious rhythmic zoning, which is characteristic of magmatic zircons (Hanchar & Rudnick, 1995), and do not present the feature of inherited zircons, generally having igneous cores, namely inherited cores, and metamorphic or recrystallization rims (Hanchar & Rudnick, 1995; Vavra *et al.* 1996). Furthermore, the Th/U ratios of zircons from the gabbro vary from 0.35 to 1.03, which is consistent with a magmatic origin (Lei *et al.* 2013). Twenty-five grains were analysed, 23 of which yield a weighted mean $^{206}Pb–^{238}U$ age of 282.2 ± 3.9 Ma (MSWD = 2.0), representing the crystallization age of this gabbro (Fig. 8a).

4.c.2. The granites

The U–Pb isotope analytical results for the zircons from a granite sample (16YG-60) are listed in Table 2. The dated sample of granite weighed 5 kg, and ~300 zircon crystals were separated from the granite. Twenty-five zircon crystals having euhedral and short columnar shapes were selected from the granite sample. They show oscillatory zoning in the CL images (Fig. 7b), which is a feature of magmatic zircons (Hanchar & Rudnick, 1995). The high Th/U ratios (0.37–1.14) of these zircon crystals also indicate that the zircons have a magmatic origin (Lei *et al.* 2013). Twenty-five analysed grains give a weighted mean $^{206}Pb–^{238}U$ age of 216.3 ± 3.2 Ma (MSWD = 2.5), which should be the granite crystallization age (Fig. 8b).

4.d. Nd–Hf isotope systems

The Nd and Hf isotope data of four gabbro samples (16YG-62–16YG-65) and four granite samples (16YG-55–16YG-58) are presented in Table 3. The εNd(t) and εHf(t) values were calculated based on the above determined zircon U–Pb ages. The gabbros show low εNd(t) values varying from −0.91 to −0.54 and positive εHf(t) values (2.59–6.37). Meanwhile, the granites are characterized by high εNd(t) values (1.55–1.99) and εHf(t) values ranging from 5.03 to 7.64.

5. Discussion

5.a. Characteristics of magma sources

5.a.1. The gabbros

The gabbros have high contents of Al, Ca, Mg and Fe and low contents of Si, K and P, suggesting a parental mantle source instead of crustal materials (Rudnick & Gao, 2003). The whole-rock εNd(t) (−0.91 to −0.54) and εHf(t) (2.59 to 6.37) values suggest derivation from an enriched mantle source or a depleted mantle source with

https://doi.org/10.1017/S0016756820000345 Published online by Cambridge University Press

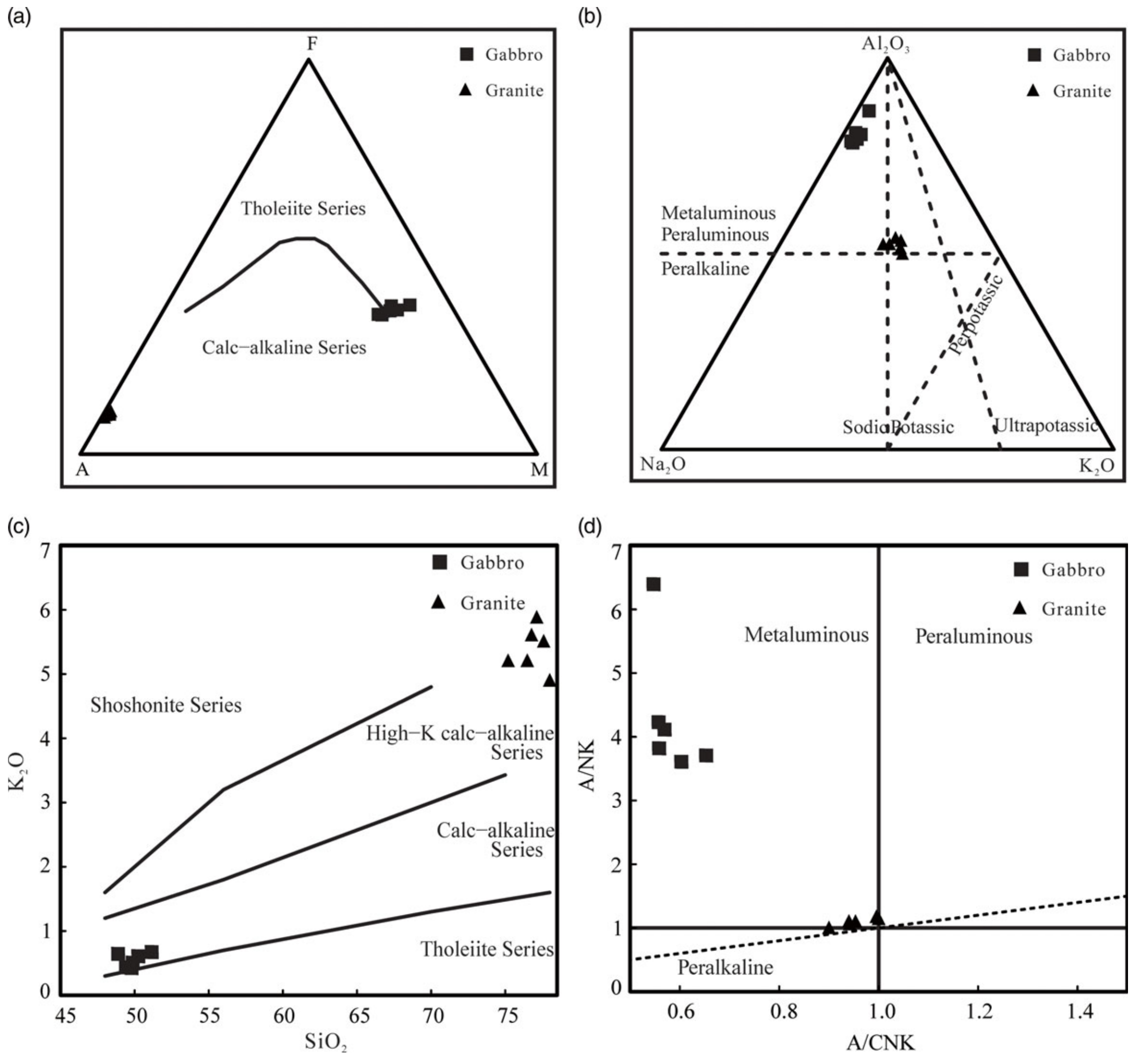

Fig. 5. (a) AFM diagram. A – $Na_2O + K_2O$; F – $FeO + Fe_2O_3$; M – MgO (Irvine & Baragar, 1971). (b) Molar Na_2O–Al_2O_3–K_2O diagram. (c) K_2O versus SiO_2 diagram (Rickwood, 1989). (d) A/NK versus A/CNK diagram (Maniar & Piccoli, 1989).

crustal contamination (Wu *et al.* 2007). First, various element ratios (e.g. Th/Yb, Th/Zr, Ce/Yb and La/Yb) sensitive to crustal contamination can indicate whether such contamination occurred during their petrogenesis (Campbell & Griffiths, 1992, 1993; Baker *et al.* 1997; Macdonald *et al.* 2001). The samples show positive correlations between Th/Yb and Th/Zr (Fig. 9a) and between Ce/Yb and La/Yb (Fig. 9b), which suggests contributions from crustal materials. Moreover, the gabbro samples have high values of Ba/Nb (69–931.59) and La/Nb (2.32–3.68) and low Ce/Pb (1.38–3.32) and Nb/U (1.51–4.85) ratios, which are all close to the continental crustal values (Jochum *et al.* 1991; Zhu *et al.* 2018). These results conform well to a derivation from depleted mantle with crustal contamination. In addition, the samples have a low SiO_2 content (49.89 %) and high Mg no. value (69), which indicate that the gabbro source was not significantly affected by the crustal materials.

On the chondrite-normalized REE diagram (Fig. 6a), the gabbros are characterized by enrichments in LREEs, which is similar to the pattern of E-MORB (Sun & McDonough, 1989). On the primitive mantle-normalized trace-element diagram (Fig. 6b), the gabbros show enrichments in LILEs and depletions in HFSEs, with markedly negative Nb–Ta and slightly negative Zr–Hf anomalies, which show arc geochemical affinities (Woodhead *et al.* 1998; Martin, 1999) and imply that the magma source was influenced by slab-derived hydrous fluids or sediment-derived melt (Davidson, 1987). The gabbro samples show high contents of Al_2O_3 (14.98–17.10 wt %) and low contents of TiO_2 (0.36–0.55 wt %) and P_2O_5 (0.06–0.13 wt %), which is different from typical within-plate basalts (WPB) but more similar to arc basalts (Zhou *et al.* 2005). Moreover, Xia *et al.* (2007) proposed that magmatic rocks influenced by subduction fluids/melts usually present low Zr contents (< 130 ppm) and Zr/Y ratios (< 4). The gabbro samples have low concentrations of Zr, with an average content of 43.07 ppm, and a low ratio of Zr/Y, at 3.44. As a result, we infer that the gabbro source underwent subduction fluid/melt metasomatism. Overall, we conclude that the magma source of the gabbro samples was depleted mantle influenced by subduction fluids/melts and slightly affected by crustal materials.

5.a.2. The granites

The granite samples have high contents of SiO_2 (75.19–78.14 wt %) and K_2O (4.92–5.87 wt %) and low contents of MgO (0.08–0.15 wt %), Al_2O_3 (11.11–12.74 wt %), TiO_2 (0.08–0.18 wt %) and P_2O_5 (0.01–0.06 wt %). They belong to the high-K calc-alkaline series and are

https://doi.org/10.1017/S0016756820000345 Published online by Cambridge University Press

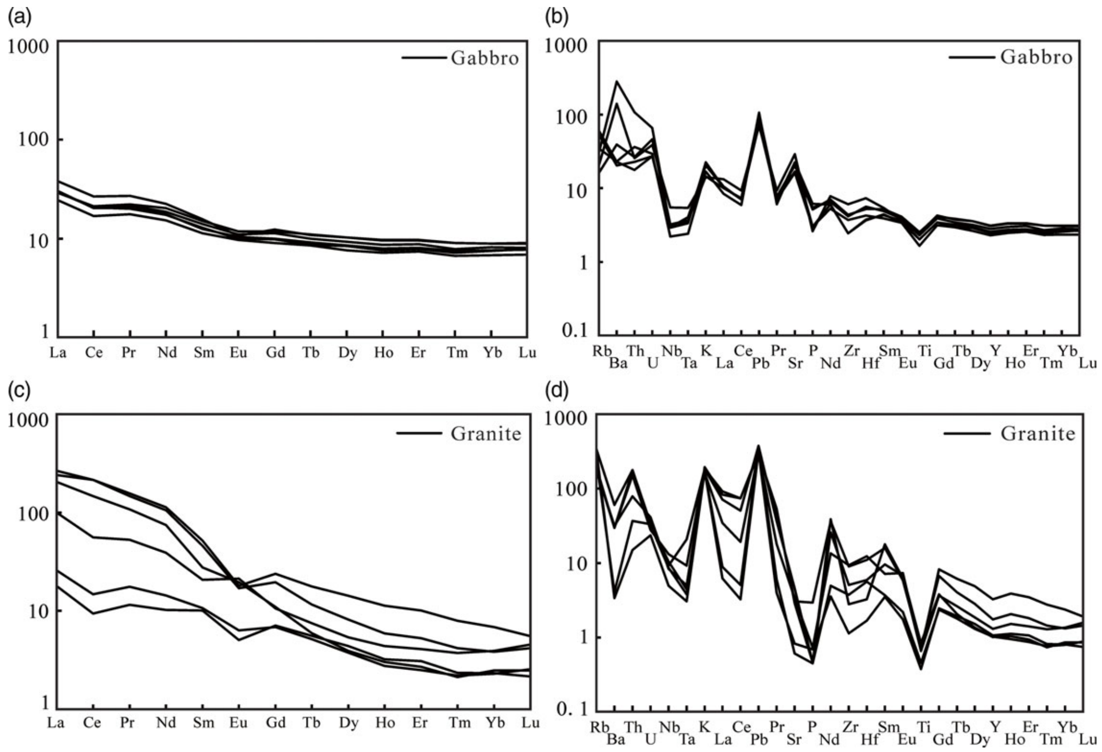

Fig. 6. Chondrite-normalized rare earth element patterns and primitive mantle-normalized multi-element diagrams of (a, b) the gabbros and (c, d) the granites, respectively. Data for chondrite and primitive mantle are from Sun & McDonough (1989).

metaluminous to weakly peraluminous. The samples present enrichments in LREEs and LILEs (Rb and K), depletions in HFSEs (Nb, Ta and Ti) and negative Eu anomalies (0.48–0.73) except for two samples that show slightly positive Eu anomalies, which is probably related to the existence of plagioclase crystals in their mineralogical composition. The 10000*Ga/Al ratios are high, ranging from 2.55 to 3.52. Furthermore, the granites have low Rb contents (< 220 ppm) and high Zr saturation temperatures (954–1131 °C) (Miller *et al.* 2003). There features are more similar to those of A-type granites. On some discrimination diagrams for A-type granites (Fig. 10), the samples plot mainly in the A-type field. Therefore, we conclude that these rocks are A-type granites (Jia *et al.* 2009). The whole-rock Nd–Hf isotope compositions can be used to constrain the source and petrogenesis of these magmatic rocks (Li *et al.* 2013). The granite samples in the study area have relatively high values of εNd(t) (1.55–1.99), which are different from the Precambrian basement rocks with markedly negative εNd(t) values (−11) in the area of the Yagan MCC (Wang *et al.* 2004). These results suggest a crust–mantle magma mixing process in their petrogenesis. In addition, they have positive εHf(t) values (5.03–7.64), which indicate contributions from mantle materials (Wu *et al.* 2007). Wang *et al.* (2002) documented a mylonitic potassic granitic pluton with a zircon U–Pb isotope age of 228 Ma in the area of the Yagan MCC, which shows the characteristics of A-type granite and was derived from the mixing of mantle and crust sources. Overall, the parental magma of the granites was most likely derived from mixing crust and mantle materials.

5.b. Tectonic setting

5.b.1. The gabbros

The tectonic setting during the formation of the early Permian magmatic rocks in the north of the ZHTZ remains controversial. Some authors suggested an active continental margin setting (Wu *et al.* 1998; Liu *et al.* 2018), whereas others argued for a postcollisional setting (Dang *et al.* 2011; Zheng *et al.* 2013; Zhang *et al.* 2017; Fei *et al.* 2019). This controversy partly results from insufficient petrogenetic constraints on the coeval mafic magmatic rocks that are more sensitive in defining key phases of tectonic environments compared to felsic rocks. We suggest that the gabbros should have formed in an active continental margin tectonic setting. In the field, the gabbros scattered within the study area have been strongly deformed, showing orientation of plagioclase and clinopyroxene to some extent. They formed dykes, most of which are cut by normal faults resulting from the extensional deformation of the crust in this region (Fig. 2; Zheng & Zhang, 1994; Wang & Zheng, 2002; Wang *et al.* 2002). That implies that the formation of the gabbro plutons was prior to the extensional event occurring after the closure of the PAO in study area. The geochemical compositions of gabbro samples can be used to indicate their tectonic setting. Wang *et al.* (2016) proposed that arc basalts are characterized by prominent negative Zr–Hf and positive Sr anomalies on primitive mantle-normalized trace-element patterns. The gabbros have these signatures that are different from arc-like continental basalts. Arc basalts can be distinguished from arc-like intracontinental basalts using various tectonic environment discrimination diagrams (Xia *et al.* 2007; Wang *et al.* 2016). All the samples plot in the fields relevant to arc basalts on these diagrams (Fig. 11). Moreover, coeval granitic rocks showing arc-like geochemical affinities have also been reported in the north of the ZHTZ (Liu, 2015; Ren, 2015; Yan *et al.* 2015; Liu *et al.* 2018). For example, the 298–290 Ma granitic rocks located near the Guaizihu area were generated by magma mixing and formed in a subduction setting (Liu *et al.* 2018). Finally, Wu (2014) argued that southward subduction, recorded by andesites, occurred in

Table 2. The zircon U–Pb dating results for the gabbro (YG-66) and the granite (16YG-60), determined by LA-ICP-MS

		Ratio						Age (Ma)			
Sample	Th/U	$^{207}Pb/^{206}Pb$	1σ	$^{207}Pb/^{235}U$	1σ	$^{206}Pb/^{238}U$	1σ	$^{207}Pb/^{235}U$	1σ	$^{206}Pb/^{238}U$	1σ
YG-66-01	0.39	0.05937	0.00122	0.36613	0.00912	0.04706	0.00111	317	7	296	7
YG-66-02	0.69	0.05162	0.00103	0.34097	0.00827	0.04532	0.00106	298	6	286	7
YG-66-03	0.59	0.05173	0.00105	0.35416	0.00868	0.04493	0.00105	308	7	283	6
YG-66-04	0.59	0.05197	0.00104	0.35272	0.00855	0.04778	0.00112	307	6	301	7
YG-66-05	1.03	0.05477	0.00114	0.36088	0.00911	0.04569	0.00107	313	7	288	7
YG-66-06	0.64	0.05126	0.00104	0.35027	0.00857	0.04732	0.00111	305	6	298	7
YG-66-07	0.74	0.05496	0.00111	0.35143	0.00860	0.04521	0.00106	306	6	285	7
YG-66-08	0.63	0.05068	0.00102	0.31859	0.00775	0.04456	0.00104	281	6	281	6
YG-66-09	0.35	0.05444	0.00270	0.37997	0.01649	0.05062	0.00121	327	12	318	7
YG-66-10	0.76	0.05172	0.00103	0.32542	0.00782	0.04401	0.00103	286	6	278	6
YG-66-11	0.61	0.05413	0.00110	0.35814	0.00871	0.04660	0.00108	311	7	294	7
YG-66-12	0.48	0.05185	0.00116	0.36404	0.00983	0.04514	0.00105	315	7	285	6
YG-66-13	0.59	0.05163	0.00104	0.34130	0.00829	0.04522	0.00105	298	6	285	6
YG-66-14	0.51	0.05301	0.00108	0.34095	0.00834	0.04372	0.00102	298	6	276	6
YG-66-15	0.51	0.05206	0.00105	0.31534	0.00759	0.04420	0.00103	278	6	279	6
YG-66-16	0.36	0.04892	0.00100	0.33345	0.00811	0.04490	0.00104	292	6	283	6
YG-66-17	0.50	0.05117	0.00103	0.33432	0.00808	0.04515	0.00105	293	6	285	6
YG-66-18	0.62	0.05336	0.00108	0.33388	0.00808	0.04354	0.00101	293	6	275	6
YG-66-19	0.61	0.05134	0.00104	0.32086	0.00775	0.04282	0.00099	283	6	270	6
YG-66-20	0.42	0.04902	0.00099	0.28729	0.00693	0.04261	0.00098	256	5	269	6
YG-66-21	0.38	0.05267	0.00108	0.33447	0.00819	0.04445	0.00103	293	6	280	6
YG-66-22	0.48	0.05342	0.00111	0.31607	0.00780	0.04197	0.00097	279	6	265	6
YG-66-23	0.41	0.05521	0.00112	0.31950	0.00770	0.04125	0.00095	282	6	261	6
YG-66-24	0.82	0.05230	0.00106	0.33325	0.00804	0.04391	0.00101	292	6	277	6
YG-66-25	0.48	0.05514	0.00114	0.35248	0.00864	0.04658	0.00107	307	6	293	7
YG-60-1	0.37	0.05087	0.00104	0.25842	0.00623	0.03661	0.00084	233	5	232	5
YG-60-2	0.45	0.05050	0.00103	0.25077	0.00603	0.03568	0.00082	227	5	226	5
YG-60-3	0.63	0.05013	0.00102	0.25328	0.00610	0.03520	0.00081	229	5	223	5
YG-60-4	0.98	0.04614	0.00095	0.23470	0.00567	0.03505	0.00080	214	5	222	5
YG-60-5	0.85	0.05184	0.00106	0.25995	0.00624	0.03490	0.00080	235	5	221	5
YG-60-6	0.49	0.05137	0.00104	0.25380	0.00606	0.03413	0.00078	230	5	216	5
YG-60-7	1.07	0.05223	0.00107	0.26762	0.00642	0.03489	0.00080	241	5	221	5
YG-60-8	0.94	0.05090	0.00104	0.23275	0.00558	0.03306	0.00075	212	5	210	5
YG-60-9	0.67	0.05312	0.00109	0.26722	0.00642	0.03514	0.00080	240	5	223	5
YG-60-10	0.72	0.04822	0.00099	0.23772	0.00571	0.03390	0.00077	217	5	215	5
YG-60-11	0.83	0.05133	0.00105	0.23939	0.00574	0.03463	0.00079	218	5	219	5
YG-60-12	1.12	0.05174	0.00107	0.24692	0.00598	0.03343	0.00076	224	5	212	5
YG-60-13	0.94	0.05341	0.00110	0.25271	0.00609	0.03312	0.00075	229	5	210	5
YG-60-14	1.04	0.05253	0.00110	0.24953	0.00607	0.03423	0.00078	226	5	217	5
YG-60-15	0.66	0.05359	0.00110	0.26318	0.00631	0.03405	0.00077	237	5	216	5
YG-60-16	1.14	0.05031	0.00103	0.23321	0.00555	0.03282	0.00074	213	5	208	5
YG-60-17	0.81	0.05166	0.00108	0.24002	0.00581	0.03180	0.00072	218	5	202	4

(*Continued*)

https://doi.org/10.1017/S0016756820000345 Published online by Cambridge University Press

Table 2. (*Continued*)

Sample	Th/U	Ratio						Age (Ma)			
		$^{207}Pb/^{206}Pb$	1σ	$^{207}Pb/^{235}U$	1σ	$^{206}Pb/^{238}U$	1σ	$^{207}Pb/^{235}U$	1σ	$^{206}Pb/^{238}U$	1σ
YG-60-18	0.48	0.05286	0.00109	0.26984	0.00649	0.03551	0.0008	243	5	225	5
YG-60-19	0.62	0.04908	0.00103	0.23600	0.00573	0.03330	0.00075	215	5	211	5
YG-60-20	0.73	0.05106	0.00109	0.23557	0.0058	0.03291	0.00074	215	5	209	5
YG-60-21	0.59	0.04970	0.00103	0.23056	0.00554	0.03227	0.00073	211	5	205	5
YG-60-22	0.90	0.05162	0.00107	0.24359	0.00583	0.03276	0.00074	221	5	208	5
YG-60-23	1.02	0.04762	0.00099	0.23834	0.00573	0.03408	0.00077	217	5	216	5
YG-60-24	0.53	0.05026	0.00104	0.25916	0.0062	0.03562	0.0008	234	5	226	5
YG-60-25	0.91	0.04892	0.00102	0.24911	0.00598	0.03504	0.00079	226	5	222	5

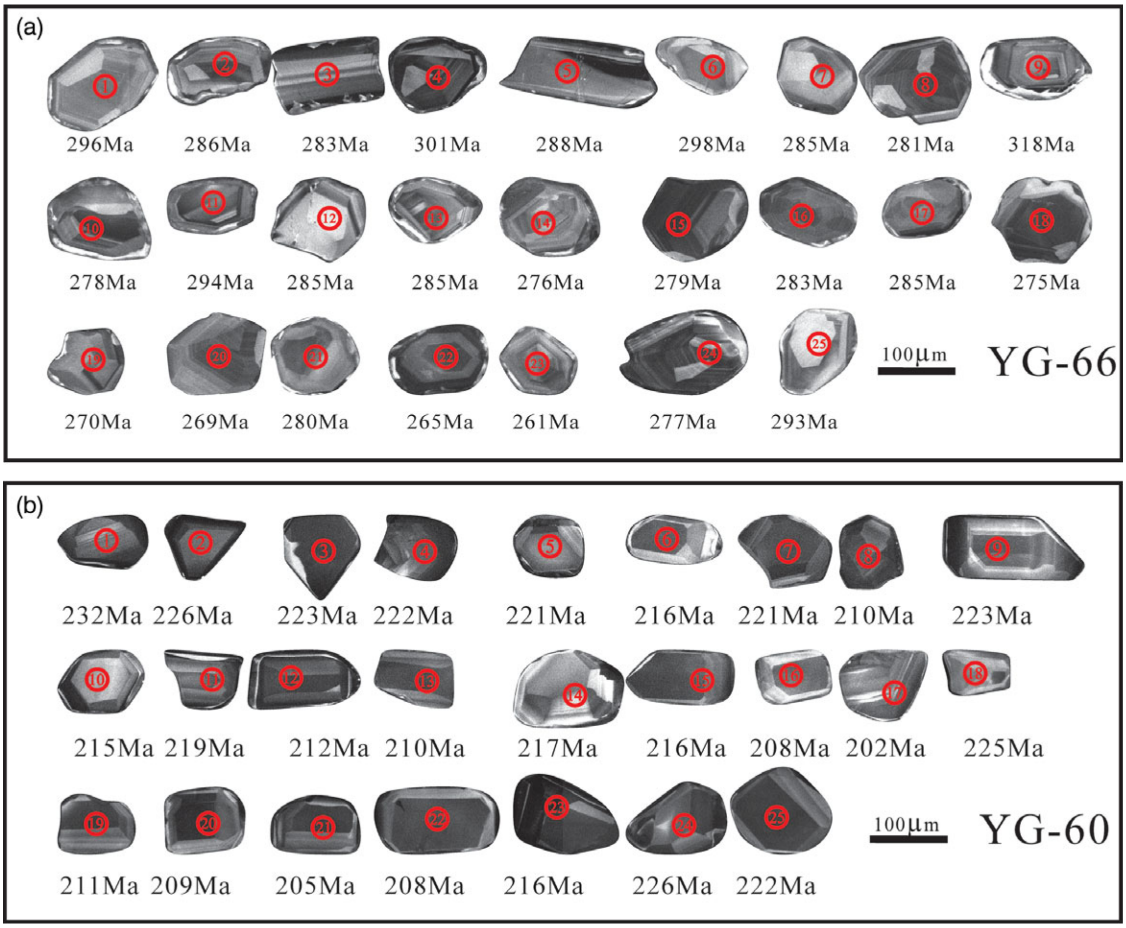

Fig. 7. (Colour online) Cathodoluminescence (CL) images of zircons from (a) the gabbro and (b) the granite.

the Mongolia–China border area during late Carboniferous to early Permian times. In conclusion, the early Permian gabbros are interpreted to represent an active continental margin tectonic setting.

5.b.2. The granites

We suggest that the granites formed in a postcollisional setting. Various tectonic setting discrimination diagrams can be used to infer the tectonic environment of the granites. All the samples plot in the postorogenic granite field on the Al_2O_3 versus SiO_2 and $FeO_t/(FeO_t + MgO)$ versus SiO_2 diagrams (Fig. 12a, b). Moreover, the granites also plot in the postorogenic granite field on the R_1 versus R_2 diagram (Fig. 12c). The granite samples plot in the volcanic arc granite (VAG) or syncollisional granite (syn-COLG) areas on the Rb versus Y + Nb diagram (Fig. 12d). Pearce (1996*b*) proposed that the Rb versus (Nb + Y) diagram reflects the sources of granites and that variable mixtures of mantle- and crust-derived magmas may cause the postcollisional granites to plot in the VAG or syn-COLG

Table 3. Nd–Hf isotopic compositions of the granites and the gabbros, determined by MC-ICP-MS

Sample	$^{147}Sm/^{144}Nd$	$^{143}Nd/^{144}Nd$ (2δ)	$f_{Sm/Nd}$	εNd(t)	T_{DM1} (Ma)	T_{DM2} (Ma)	$^{176}Lu/^{177}Hf$	$^{176}Hf/^{177}Hf$ (2δ)	$f_{lu/Hf}$	εHf(t)	T_{DM1} (Ma)	T_{DM2} (Ma)
YG-55	0.090523	0.512590 ± 3	−0.54	1.99	696	833	0.020163	0.282861 ± 5	−0.39	5.03	1129	929
YG-56	0.195063	0.512738 ± 8	−0.01	1.99	3371	833	0.015154	0.282903 ± 7	−0.54	7.22	794	790
YG-57	0.146741	0.512647 ± 6	−0.25	1.55	1149	870	0.005377	0.282875 ± 6	−0.84	7.64	604	763
YG-58	0.105142	0.512604 ± 2	−0.47	1.87	769	843	0.004340	0.282841 ± 5	−0.87	6.58	639	830
YG-62	0.146300	0.512514 ± 4	−0.26	−0.61	1441	1099	0.017958	0.282765 ± 7	−0.46	2.59	1257	1134
YG-63	0.146773	0.512518 ± 3	−0.25	−0.54	1441	1093	0.005970	0.282784 ± 8	−0.82	5.52	764	949
YG-64	0.148082	0.512501 ± 3	−0.25	−0.91	1509	1124	0.005774	0.282807 ± 10	−0.83	6.37	722	895
YG-65	0.137926	0.512494 ± 4	−0.30	−0.70	1322	1106	0.007362	0.282777 ± 8	−0.78	5.00	810	981

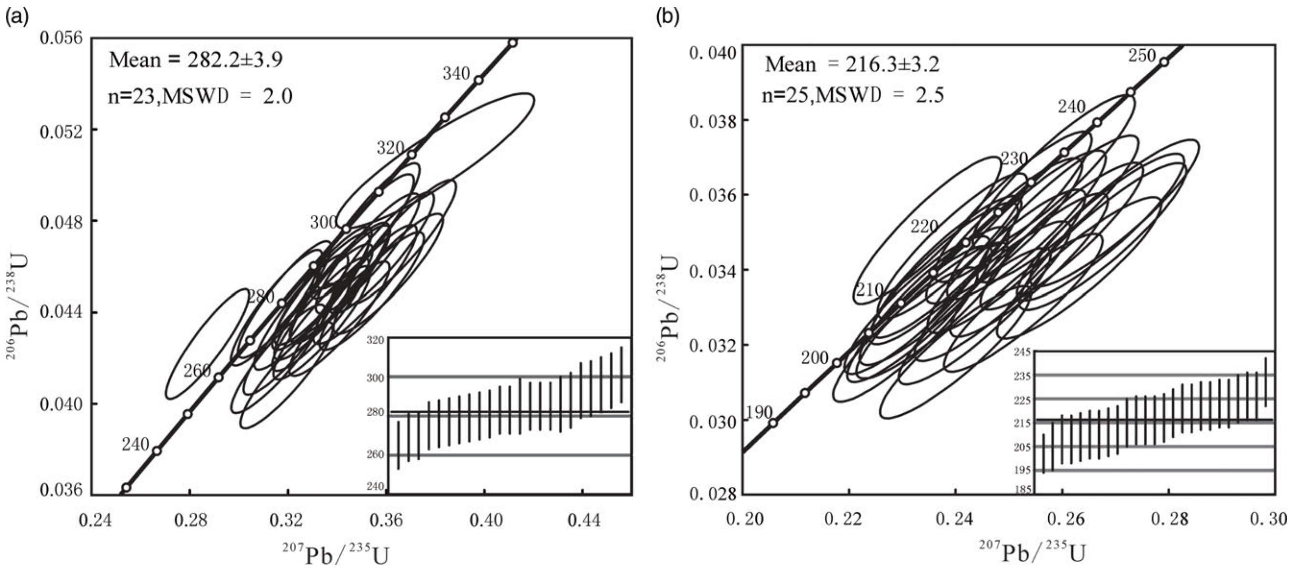

Fig. 8. U–Pb concordia diagrams for zircons from (a) the gabbro and (b) the granite.

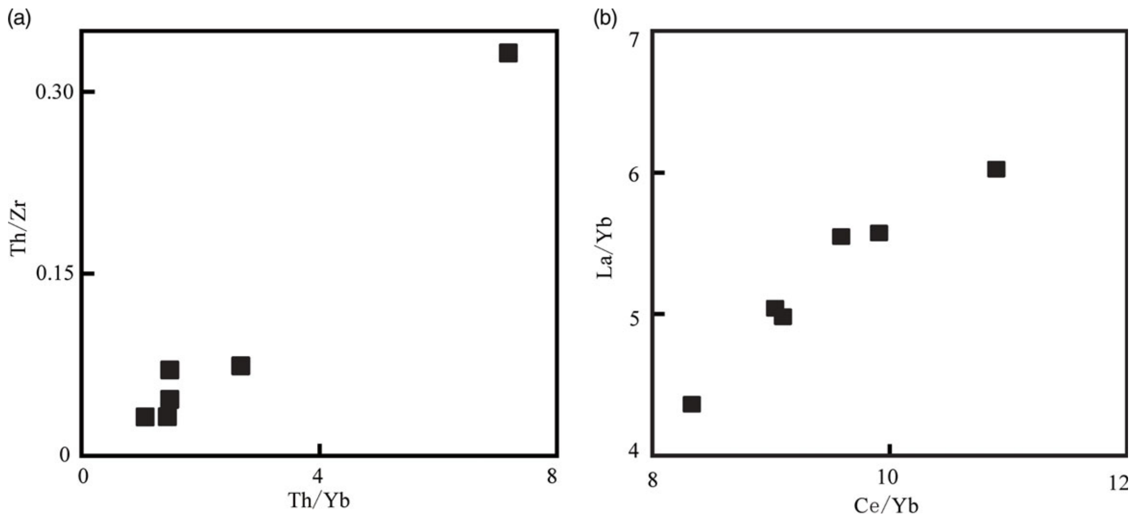

Fig. 9. (a) Th/Zr versus Th/Yb and (b) La/Yb versus Ce/Yb diagrams for the gabbros.

https://doi.org/10.1017/S0016756820000345 Published online by Cambridge University Press

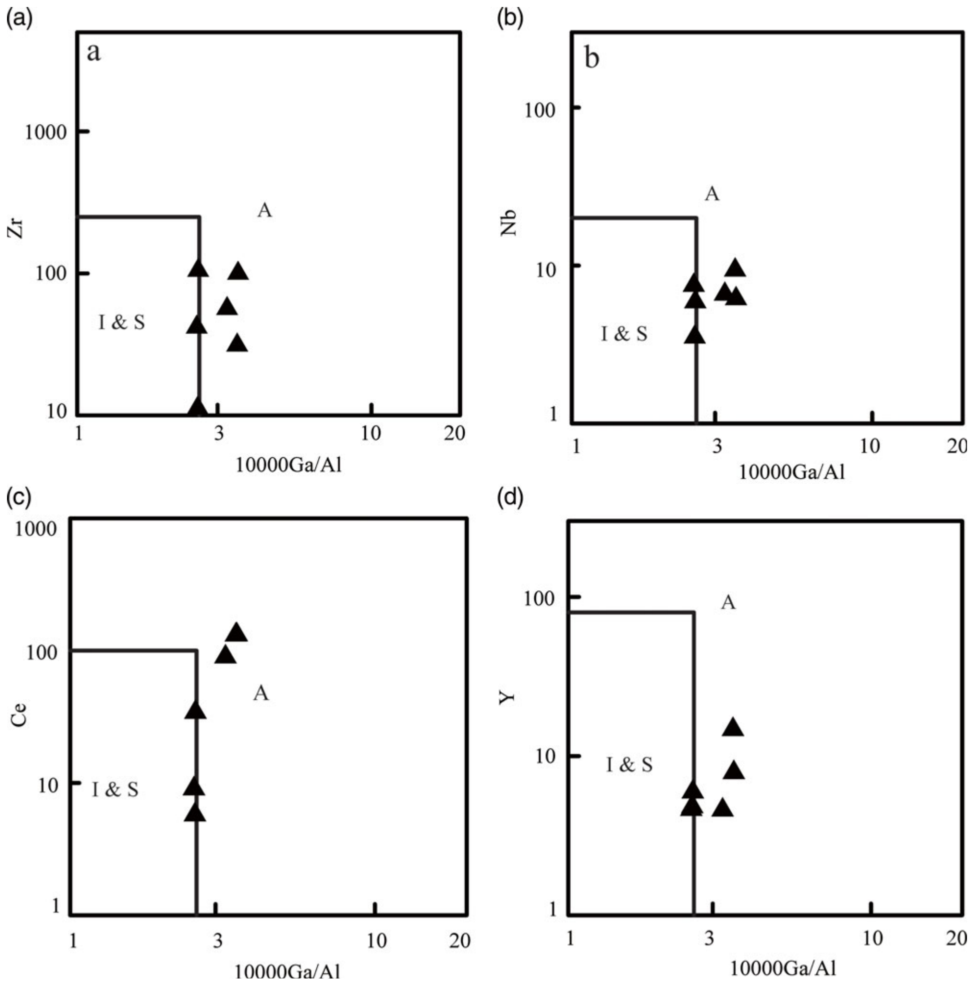

Fig. 10. Chemical classification diagrams: (a) Zr versus 10000Ga/Al; (b) Nb versus 10000Ga/Al; (c) Ce versus 10000Ga/Al; (d) Y versus 10000Ga/Al (after Whalen *et al.* 1987).

areas. Furthermore, previous studies that focused on voluminous early Mesozoic granitic rocks exposed in the area of the Yagan MCC (Wang *et al.* 2002, 2004) and its adjacent areas, including Beishan (Li *et al.* 2012, 2013), suggested that these granitic rocks were generated in a postcollisional setting after the closure of the PAO. These features suggest that the granites formed in a post-collisional tectonic setting. In addition, the granites intrude the Precambrian metamorphic rocks in the area of the Yagan MCC along normal faults, which developed as a result of the extensional deformation of the crust in this area (Zheng & Zhang, 1994). The granite samples have been strongly deformed, showing foliation and lineations parallel to the regional extensional shearing. The lineations are defined by compositional banding of both K-feldspar and quartz crystals, which is characteristic of syntectonic granites experiencing syn-emplacement extensional deformation (Wang *et al.* 2002). We infer that the collisional event resulting from the closure of the PAO during late Permian to Early–Middle Triassic times caused crustal thickening in the Yagan MCC area and that delamination of the mantle lithosphere subsequently took place. Upwelling asthenosphere ascended to shallow mantle depths and generated mafic magmas that provided heat and materials to the crust; then, the mantle- and crust-derived magmas mixed (Liu *et al.* 2018). The extensional faults started to develop as the magma was emplaced upwards. This explanation is also consistent with the sedimentary records in the Yagan MCC area. In conclusion, we infer that the Late Triassic granites should have formed in a post-collisional tectonic setting.

5.c. Tectonic implications for the northern Alxa area

The study area is situated in the north of the ZHTZ. In early Palaeozoic time, the region was probably a passive continental margin, because this area received continuous sedimentation of clastic rocks accompanied by carbonate rocks with abundant *Dalmanites* fossils (Wu & He, 1993). However, volcanic activity occurred during late Palaeozoic time. As a result, the region was transformed into an active continental margin during late Palaeozoic time (Wu *et al.* 1998; Zheng *et al.* 2013).

Based on the geochemical and geochronological characteristics of the magmatic rocks exposed in the northern Alxa area, some authors argued that the late Palaeozoic volcanic activity in this region was related to the northward subduction of the PAO represented by the Enger Us ophiolitic belt (Liu *et al.* 2016, 2017; Zhang *et al.* 2017). The Enger Us ophiolitic belt is widely accepted to represent the major suture of the PAO in the Alxa area, and the Quagan Qulu ophiolitic belt represents a back-arc basin. These two ophiolitic belts, together with the arc in the ZSTZ, are considered a late Palaeozoic ocean–arc–back-arc basin system related to the southward subduction of the PAO represented by the Enger Us ophiolitic belt (Zheng *et al.* 2014). However, no evidence, such as tectonic deformation, magmatic activity or the sedimentary record, supports the northward subduction of the PAO represented by the Enger Us ophiolitic belt. Therefore, we conclude that the southward subduction of the PAO represented by the Yagan Fault Belt, which is located to the north of the study area and represents an

https://doi.org/10.1017/S0016756820000345 Published online by Cambridge University Press

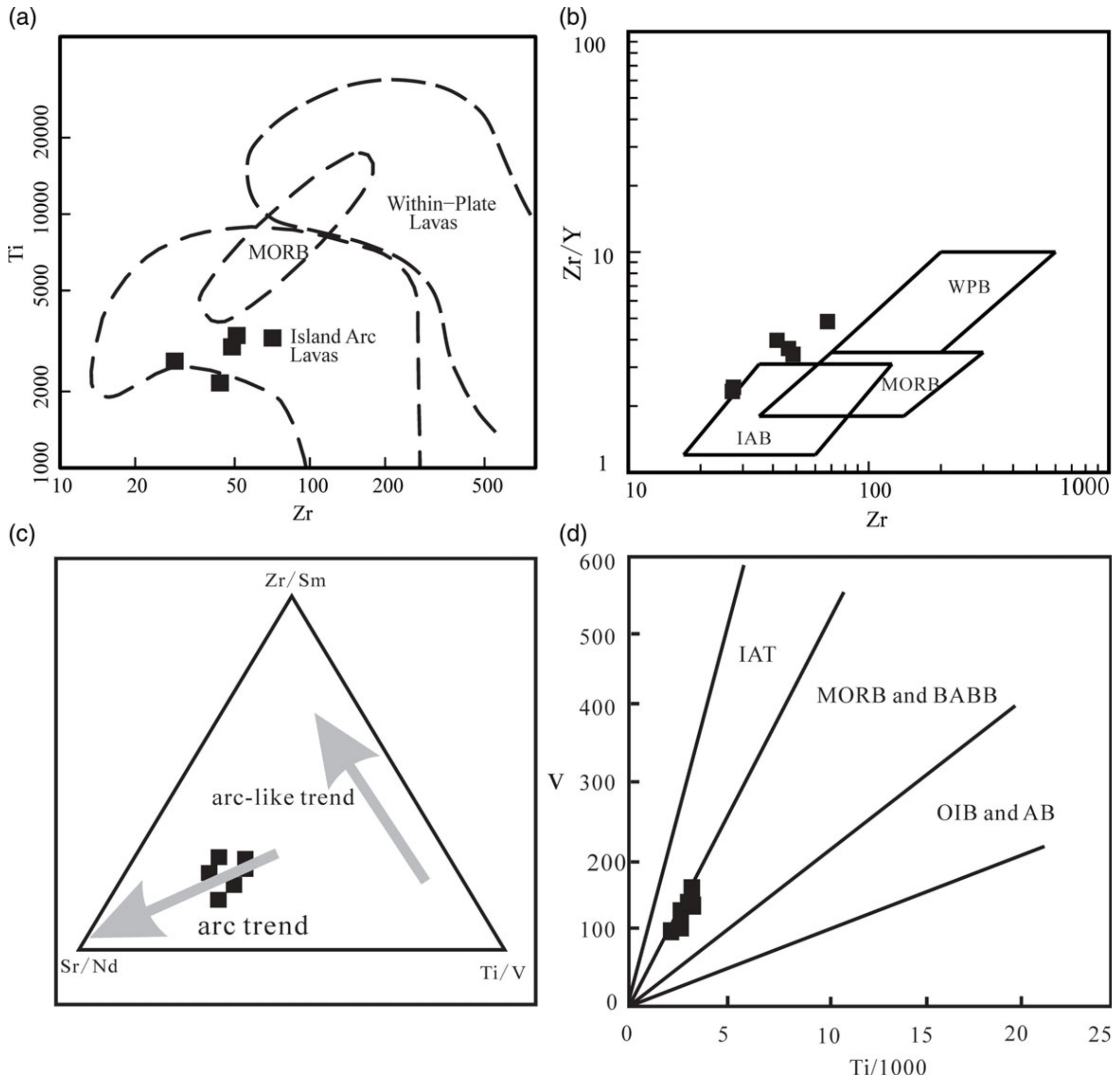

Fig. 11. Tectonic environment discrimination diagrams for the gabbros: (a) Ti versus Zr (Pearce, 1996*a*); (b) Zr/Y versus Zr (Pearce & Norry, 1979); (c) Zr/Sm–Sr/Nd–Ti/V (Wang *et al.* 2016); (d) V versus Ti (Shervais, 1982). MORB – mid-ocean ridge basalts; WPB – within-plate basalts; IAB – island-arc basalts; IAT – island-arc tholeiites; BABB – back-arc basin basalts; OIB – ocean-island basalts; AB – alkali basalts.

important boundary according to the comparable lithologies on the southern and northern flanks of the boundary (Zhang *et al.* 2017; Liu *et al.* 2018), occurred during late Palaeozoic time and was responsible for the late Palaeozoic volcanic activity in the northern ZHTZ.

Zhang *et al.* (2017) documented a Late Devonian monzogranite in the Wudenghan area (Fig. 1b), which is located in the northern ZHTZ, and thought that it probably represents a highly fractionated VAG. Fan (2015) proposed that the late Carboniferous volcanic rocks in the Guaizihu area (Fig. 1b) formed in an active continental margin setting. Combining our results with those of previous studies, we conclude that the oceanic crust represented by the Yagan Fault Belt began to subduct southwards beneath the study area at least in Late Devonian time and that the southward subduction still occurred in early Permian time, as proven by the gabbros in this study and other coeval granitic rocks showing arc-like geochemical affinities. Furthermore, the final closure of the ocean more likely occurred in late Permian to Early–Middle Triassic times. First, in the study area, the extensional structure recorded by the Yagan MCC occurred in Late Triassic time (Wang *et al.* 2002). Second, the Late Triassic granitic rocks exposed in the study area and adjacent regions, including Beishan, formed in a post-collisional setting (Wang *et al.* 2002; Li *et al.* 2012, 2013). Moreover, the study area is the southern continuation of the Tsagaan Uul terrane (Wang *et al.* 2001), which may represent part of the South Gobi microcontinent (Badarch *et al.* 2002). Heumann *et al.* (2012) argued that the Permian and Triassic deposits in the terrane contain a sedimentary record of the final closure of the PAO, which appears to support the late Permian to Early–Middle Triassic amalgamation between the YTZ and the north of the ZHTZ. The upper Permian rocks experienced folding and lower greenschist-facies metamorphism, while the Upper Triassic rocks are characterized by terrestrial redbeds and conglomerates and did not experience regional metamorphism (Zheng & Zhang, 1994; Johnson *et al.* 2008; Heumann *et al.* 2012). Overall, the PAO represented by the Yagan Fault Belt started to subduct southwards at least by Late Devonian time, and the timing of the final closure of the ocean should be the late Permian to Early–Middle Triassic period.

In conclusion, the late Permian to Early–Middle Triassic was a critical period marking the timing of the final closure of the PAO in

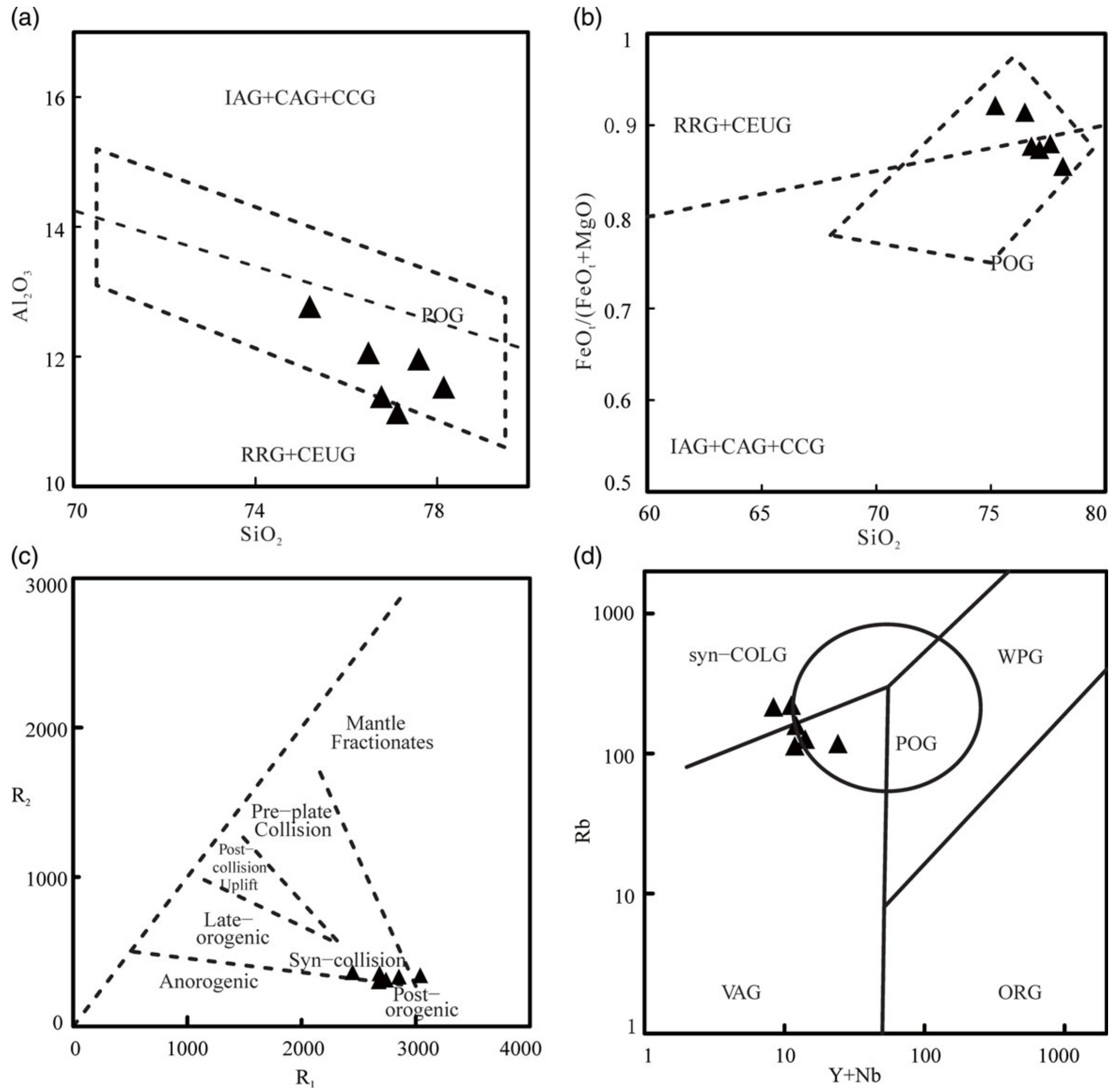

Fig. 12. Tectonic environment discrimination diagrams for the granites: (a) Al_2O_3 versus SiO_2; (b) $FeO_t/(FeO_t + MgO)$ versus SiO_2 (after Maniar & Piccoli, 1989); (c) R_1 versus R_2 (after Batchelor & Bowden, 1985); (d) Rb versus Y + Nb (Pearce, 1996*b*). IAG – island arc granite; CAG – continental arc granite; CCG – continental collisional granite; POG – post-orogenic granite; RRG – rift-related granite; CEUG – continental epeirorgenic uplift granite; WPG – within-plate granite; VAG – volcanic arc granite; syn-COLG – syncollisional granite; ORG – oceanic ridge granite.

the northern Alxa area. This inference agrees with integrated magmatic, structural and sedimentary studies in the northern Alxa area. Therefore, we infer that the final closure of the branch of the PAO in the northern Alxa area took place during late Permian to Early–Middle Triassic times. This study does not support the interpretation that the PAO finally closed in Late Devonian–Permian times but instead implies that the final closure of the central part of the PAO in the southern CAOB took place in late Permian to Early–Middle Triassic times.

6. Conclusions

(1) The early Permian gabbros were derived from a depleted mantle source metasomatized by subduction fluids/melts, and crustal contamination was involved during the processes of magma migration and emplacement. The gabbros probably formed in an active continental margin tectonic setting in response to the southward subduction of oceanic crust represented by the Yagan Fault Belt.

(2) The Late Triassic granites were derived from the mixing of mantle and crustal materials. These granites formed in a post-collisional tectonic setting following the closure of the ocean represented by the Yagan Fault Belt. The area in the northern ZHTZ entered the postcollisional extensional stage in Late Triassic time.

(3) In early Palaeozoic time, the area in the northern ZHTZ was a passive continental margin. At least by Late Devonian time, the region changed to an active continental margin in response to the southward subduction of the branch of the PAO represented by the Yagan Fault Belt. The final closure of the PAO in the central part of the southern CAOB occurred in late Permian to Early–Middle Triassic times.

Acknowledgements. The study is supported by the Fundamental Research Funds for the Central Universities (No. Lzujbky-2018-it20) and the China Geological Survey (No. 121201011000161111-01).

References

Andersen T (2002) Correction of common lead in U–Pb analyses that do not report ^{204}Pb. *Chemical Geology* **192**, 59–79.

Badarch G, Cunningham WD and Windley BF (2002) A new terrane subdivision for Mongolia: implications for the Phanerozoic crustal growth of Central Asia. *Journal of Asian Earth Sciences* **21**, 87–110.

Baker JA, Menzies MA, Thirlwall MF and MacPherson CG (1997) Petrogenesis of Quaternary intraplate volcanism, Sana'a, Yemen: implications for plume–lithosphere interaction and polybaric melt hybridization. *Journal of Petrology* **38**, 1359–90.

Batchelor RA and Bowden P (1985) Petrogenetic interpretation of granitoid rock series using multicationic parameters. *Chemical Geology* **48**, 43–55.

BGNHAR (Bureau of Geology, Ningxia Hui Autonomous Region) (1982) *Hariaoribuerge Sheet*. Regional Geological Survey Report (1:200000) (in Chinese).

Campbell IH and Griffiths RW (1992) The changing nature of mantle hotspots through time: implications for the chemical evolution of the mantle. *The Journal of Geology* **100**, 497–523.

Campbell IH and Griffiths RW (1993) The evolution of the mantle's chemical structure. *Lithos* **30**, 389–99.

Charvet J, Shu LS, Laurent-Charvet S, Wang B, Faure M, Cluzel D, Chen Y and De Jong K (2011) Palaeozoic tectonic evolution of the Tianshan belt, NW China. *Science China Earth Sciences* **54**, 166–84.

Dang B, Zhao H, Lin GC, Wu KL, Kang XY, Ge HY, Wu B and Liu SH (2011) Geochemistry and tectonic setting of Permian volcanic rocks in Yingen-Ejin Banner basin and its neighboring areas, western Inner Mongolia. *Geological Bulletin of China* **30**, 923–31 (in Chinese with English abstract).

Davidson JP (1987) Crustal contamination versus subduction zone enrichment: examples from the Lesser Antilles and implications for mantle source compositions of island arc volcanic rocks. *Geochimica et Cosmochimica Acta* **51**, 2185–98.

Fan CF (2015) *Study on the volcanic rocks of the Baishan formation in the Carboniferous in the Guaizi lake area of the Inner Mongolia*. M.Sc. thesis, Chang'an University, Xian, China. Published thesis.

Fei MM, Pan M, Xie CL, Wang JH and Zhao HS (2019) Timing and tectonic settings of the Late Paleozoic intrusions in the Zhusileng, northern Alxa: implication for the metallogeny. *Geosciences Journal* **23**, 37–57.

Feng JY, Xiao WJ, Windley BF, Han CM, Wan B, Zhang JE, Ao SJ, Zhang ZY and Lin LN (2013) Field geology, geochronology and geochemistry of mafic-ultramafic rocks from Alxa, China: implications for Late Permian accretionary tectonics in the southern Altaids. *Journal of Asian Earth Sciences* **78**, 114–42.

Han BF, Guo ZJ and He GQ (2010) Timing of major suture zones in North Xinjiang, China: constraints from stitching plutons. *Acta Petrologica Sinica* **26**, 2233–46.

Hanchar JM and Rudnick RL (1995) Revealing hidden structures: the application of cathodoluminescence and back-scattered electron imaging to dating zircons from lower crustal xenoliths. *Lithos* **36**, 289–303.

Heumann MJ, Johnson CL, Webb LE, Taylor JP, Jalbaa U and Minjin C (2012) Paleogeographic reconstruction of a late Paleozoic arc collision zone, southern Mongolia. *Geological Society of America Bulletin* **124**, 1514–34.

Irvine TN and Baragar WRA (1971) A guide to the chemical classification of the common volcanic rocks. *Canadian Journal of Earth Sciences* **8**, 523–48.

Jahn BM, Wu FY and Chen B (2000) Granitoids of the Central Asian Orogenic Belt and continental growth in the Phanerozoic. *Transactions of the Royal Society of Edinburgh: Earth Sciences* **91**, 181–93.

Jia XH, Wang Q and Tang GJ (2009) A-type granites: research progress and implications. *Geotectonica et Metallogenia* **33**, 465–80.

Jochum KP, Arndt NT and Hofmann AW (1991) Nb–Th–La in komatiites and basalts: constraints on komatiite petrogenesis and mantle evolution. *Earth and Planetary Science Letters* **107**, 272–89.

Johnson C, Amory J, Zinniker D, Lamb M, Graham SA, Affolter M and Badarch G (2008) Sedimentary response to arc-continent collision, Permian, southern Mongolia. In *Formation and Applications of the Sedimentary Record in Arc Collision Zones* (eds AE Draut, PD Clift and DW Scholl), pp. 363–90. Geological Society of America, Special Paper no. 436.

Lei WY, Shi GH and Liu YX (2013) Research progress on trace element characteristics of zircons of different origins. *Earth Science Frontiers* **20**, 273–84.

Li S, Wang T, Wilde SA and Tong Y (2013) Evolution, source and tectonic significance of Early Mesozoic granitoid magmatism in the Central Asian Orogenic Belt (central segment). *Earth-Science Reviews* **126**, 206–34.

Li S, Wang T, Wilde SA, Tong Y, Hong DW and Guo QQ (2012) Geochronology, petrogenesis and tectonic implications of Triassic granitoids from Beishan, NW China. *Lithos* **134**, 123–45.

Liu QF (2015) *Petrogenesis, geochemistry and tectonic implication of Guaizihu composite rock body in Alxa of Inner Mongolia*. M.Sc. thesis, Chang'an University, Xian, China. Published thesis.

Liu Q, Zhao GC, Han YG, Eizenhöfer PR, Zhu YL, Hou WZ, Zhang XR and Wang B (2017) Geochronology and geochemistry of Permian to Early Triassic granitoids in the Alxa Terrane: constraints on the final closure of the Paleo-Asian Ocean. *Lithosphere* **9**, 665–80.

Liu Q, Zhao GC, Han YG, Li XP, Zhu YL, Eizenhöfer PR, Zhang XR, Wang B and Tsui RW (2018) Geochronology and geochemistry of Paleozoic to Mesozoic granitoids in Western Inner Mongolia, China: implications for the tectonic evolution of the southern Central Asian Orogenic Belt. *The Journal of Geology* **126**, 451–71.

Liu Q, Zhao GC, Sun M, Han YG, Eizenhöfer PR, Hou WZ, Zhang XR, Zhu YL, Wang B, Liu DX and Xu B (2016) Early Paleozoic subduction processes of the Paleo-Asian Ocean: insights from geochronology and geochemistry of Paleozoic plutons in the Alxa Terrane. *Lithos* **262**, 546–60.

Ludwig KR (2003) *User's Manual for Isoplot 3.00: A Geochronological Toolkit for Microsoft Excel*. Berkeley Geochronology Center, Special Publication no. 4.

Macdonald R, Rogera NW, Fitton JG, Black S and Smith M (2001) Plume–lithosphere interactions in the generation of the basalts of the Kenya Rift, East Africa. *Journal of Petrology* **42**, 877–900.

Maniar PD and Piccoli PM (1989) Tectonic discrimination of granitoids. *Geological Society of America Bulletin* **101**, 635–43.

Martin H (1999) Adakitic magmas: modern analogues of Archaean granitoids. *Lithos* **46**, 411–29.

Middlemost EAK (1994) Naming materials in the magma/igneous rock system. *Earth-Science Reviews* **37**, 215–24.

Miller CF, McDowell SM and Mapes RW (2003) Hot and cold granites? Implications of zircon saturation temperatures and preservation of inheritance. *Geology* **31**, 529–32.

Pearce J (1996a) A user's guide to basalt discrimination diagrams. In *Trace Element Geochemistry of Volcanic Rocks: Applications for Massive Sulphide Exploration* (ed. DA Wyman), pp. 79–113. Geological Association of Canada, Short Course Notes 12.

Pearce J (1996b) Sources and settings of granitic rocks. *International Union of Geological Sciences* **19**, 120–25.

Pearce JA and Norry MJ (1979) Petrogenetic implications of Ti, Zr, Y, and Nb variations in volcanic rocks. *Contributions to Mineralogy and Petrology* **69**, 33–47.

Pearce NJG, Perkins WT, Westgate JA, Gorton MP, Jackson SE, Neal CR and Chenery SP (1997) A compilation of new and published major and trace element data for NIST SRM 610 and NIST SRM 612 glass reference materials. *Geostandards Newsletter* **21**, 115–44.

Ren JM (2015) *Study on Permian granitoids in Dazhaganaobao, Ejinaqi, Inner Mongolia*. M.Sc. thesis, Chang'an University, Xian, China. Published thesis.

Rickwood PC (1989) Boundary lines within petrologic diagrams which use oxides of major and minor elements. *Lithos* **22**, 247–63.

Rudnick R and Gao S (2003) Composition of the continental crust. *Treatise on Geochemistry* **3**, 1–64.

Sengör AMC, Natalin BA and Burtman VS (1993) Evolution of the Altaid tectonic collage and Palaeozoic crustal growth in Eurasia. *Nature* **364**, 299–307.

Shervais JW (1982) Ti–V plots and the petrogenesis of modern and ophiolitic lavas. *Earth and Planetary Science Letters* **59**, 101–18.

Song DF, Xiao WJ, Collins AS, Glorie S, Han CM and Li Y C (2018) Final subduction processes of the Paleo-Asian Ocean in the Alxa tectonic belt (NW China): constraints from field and chronological data of Permian arc-related volcano-sedimentary rocks. *Tectonics* **37**, 1658–87.

Sun SS and McDonough WF (1989) Chemical and isotopic systematics of oceanic basalts: implications for mantle composition and processes. In *Magmatism in the Ocean Basins* (eds AD Saunders and MJ Norry), pp. 313–45. Geological Society of London, Special Publication no. 42.

Vavra G, Gebauer D, Schmid R and Compston W (1996) Multiple zircon growth and recrystallization during polyphase Late Carboniferous to Triassic metamorphism in granulites of the Ivrea Zone (Southern Alps): an ion microprobe (SHRIMP) study. *Contributions to Mineralogy and Petrology* **122**, 337–58.

Wan B, Li SH, Xiao WJ and Windley BF (2018) Where and when did the Paleo-Asian ocean form? *Precambrian Research* **317**, 241–52.

Wang TY, Liu JK, Wang SZ and Wu JH (1993) Late Paleozoic extension and tectono-magmatic evolution in the Sino-Mongolia border region in the northern part of Alxa. *Regional Geology of China* (4), 317–27 (in Chinese with English abstract).

Wang TY, Wang SZ and Wang JR (1994) *The Formation and Evolution of Paleozoic Continental Crust in Alaxa Region*. Lanzhou: Lanzhou University Press.

Wang XC, Wilde SA, Xu B and Pang CJ (2016) Origin of arc-like continental basalts: implications for deep-Earth fluid cycling and tectonic discrimination. *Lithos* **261**, 5–45.

Wang T and Zheng YD (2002) Mesozoic progressive transition from overthrusting to extension in the Sino-Mongolian border region and crustal-scale tangential shear. *Geological Bulletin of China* **21**, 232–7 (in Chinese with English abstract).

Wang T, Zheng YD, Gehrels GE and Mu ZG (2001) Geochronological evidence for existence of South Mongolian microcontinent—a zircon U–Pb age of granitoid gneisses from the Yagan-Onch Hayrhan metamorphic core complex. *Chinese Science Bulletin* **46**, 2005–8.

Wang T, Zheng YD, Li TB and Gao YJ (2004) Mesozoic granitic magmatism in extensional tectonics near the Mongolian border in China and its implications for crustal growth. *Journal of Asian Earth Sciences* **23**, 715–29.

Wang T, Zheng YD, Liu SW, Li TB and Ma MB (2002) Mylonitic potassic granitoids from the Yagan metamorphic core complex on Sino-Mongolian border: a mark of transition from contractile to extensional tectonic regime. *Acta Petrologica Sinica* **18**, 177–86 (in Chinese with English abstract).

Webb LE, Graham SA, Johnson CL, Badarch G and Hendrix MS (1999) Occurrence, age, and implications of the Yagan-Onch Hayrhan metamorphic core complex, southern Mongolia. *Geology* **27**, 143–6.

Whalen JB, Currie KL and Chappell BW (1987) A-type granites: geochemical characteristics, discrimination and petrogenesis. *Contributions to Mineralogy and Petrology* **95**, 407–19.

Wiedenbeck M, Alle P, Corfu F, Griffin WL, Meier M, Oberli F, Quadt AV, Roddick JC and Spiegel W (1995) Three natural zircon standards for U–Th–Pb, Lu–Hf, trace element and REE analyses. *Geostandards Newsletter* **19**, 1–23.

Windley BF, Alexeiev D, Xiao WJ, Kroener A and Badarch G (2007) Tectonic models for accretion of the Central Asian Orogenic Belt. *Journal of the Geological Society, London* **164**, 31–47.

Woodhead JD, Eggins SM and Johnson RW (1998) Magma genesis in the New Britain island arc: further insights into melting and mass transfer processes. *Journal of Petrology* **39**, 1641–68.

Wu GY (2014) Palinspastic reconstruction and geological evolution of Permian residual marine basins bordering China and Mongolia. *Journal of Palaeogeography* **3**, 219–32.

Wu TR and He GQ (1993) Tectonic units and their fundamental characteristics on the northern margin of the Alxa Block. *Acta Geologica Sinica* **67**, 97–108 (in Chinese with English abstract).

Wu TR, He GQ and Zhang C (1998) On Palaeozoic tectonics in the Alxa region, Inner Mongolia, China. *Acta Geologica Sinica* **72**, 256–63.

Wu FY, Li XH, Zheng YF and Gao S (2007) Lu–Hf isotopic systematics and their application in petrology. *Acta Petrologica Sinica* **23**, 185–220.

Xia LQ, Xia ZC, Xu XY, Li XM and Ma ZP (2007) The discrimination between continental basalt and island arc basalt based on geochemical method. *Acta Petrologica et Mineralogica* **26**, 77–89.

Xiao WJ, Song DF, Windley BF, Li JL, Han CM, Wan B, Zhang JE, Ao SJ and Zhang ZY (2019) Research progresses of the accretionary processes and metallogenesis of the Central Asian Orogenic Belt. *Science China Earth Sciences* **11**, 14–19.

Xiao WJ, Windley BF, Hao J and Zhai MG (2003) Accretion leading to collision and the Permian Solonker suture, Inner Mongolia, China: termination of the central Asian orogenic belt. *Tectonics* **22**, doi: 10.1029/2002TC001484.

Xiao WJ, Windley BF, Huang BC, Han CM, Yuan C, Chen HL, Sun M, Sun S and Li JL (2009) End-Permian to mid-Triassic termination of the accretionary processes of the southern Altaids: implications for the geodynamic evolution, Phanerozoic continental growth, and metallogeny of Central Asia. *International Journal of Earth Sciences* **98**, 1189–217.

Xiao WJ, Windley BF, Sun S, Li JL, Huang BC, Han CM, Yuan C, Sun M and Chen HL (2015) A tale of amalgamation of three Permo-Triassic collage systems in Central Asia: oroclines, sutures, and terminal accretion. *Annual Review of Earth and Planetary Sciences* **43**, 477–507.

Xiao WJ, Zhang LC, Qin KZ, Sun S and Li JL (2004) Paleozoic accretionary and collisional tectonics of the eastern Tianshan (China): implications for the continental growth of central Asia. *American Journal of Science* **304**, 370–95.

Xu B, Charvet J, Chen Y, Zhao P and Shi G Z (2013) Middle Paleozoic convergent orogenic belts in western Inner Mongolia (China): framework, kinematics, geochronology and implications for tectonic evolution of the Central Asian Orogenic Belt. *Gondwana Research* **23**, 1342–64.

Yan HQ, Chen Y, Fan MC, Ren JM, Jiang S, Lv JL, Zhao SX and Fan CF (2015) Geochemical features and geological significance of granitoid rocks in Guaizihu, Ejinaqi, Inner Mongolia. *Strategic Study of CAE* **17**, 97–105 (in Chinese with English abstract).

Zhang W, Pease V, Meng QP, Zheng RG, Wu TR, Chen Y and Gan LS (2017) Age and petrogenesis of late Paleozoic granites from the northernmost Alxa region, northwest China, and implications for the tectonic evolution of the region. *International Journal of Earth Sciences* **106**, 79–96.

Zheng YD, Wang SZ and Wang YF (1991) An enormous thrust nappe and extensional metamorphic core complex newly discovered in Sino-Mongolian boundary area. *Science in China, Series B* **34**, 1145–54.

Zheng RG, Wu TR, Zhang W, Feng JC, Xu C, Meng QP and Zhang ZY (2013) Geochronology and geochemistry of the Yagan granite in the northern margin of the Alxa block: constraints on the tectonic evolution of the southern Altaids. *Acta Petrologica Sinica* **29**, 2665–75 (in Chinese with English abstract).

Zheng RG, Wu TR, Zhang W, Xu C, Meng QP and Zhang ZY (2014) Late Paleozoic subduction system in the northern margin of the Alxa block, Altaids: geochronological and geochemical evidences from ophiolites. *Gondwana Research* **25**, 842–58.

Zheng YD and Zhang Q (1994) The Yagan metamorphic core complex and extensional detachment fault in Inner Mongolia, China. *Acta Geologica Sinica* **7**, 125–35.

Zhou CY, Wu FY, Ge WC, Sun DY, Abdel-Rahman AA, Zhang JH and Cheng RY (2005) Age, geochemistry and petrogenesis of the cumulate gabbro in Tahe, northern Da Hinggan Mountain. *Acta Petrologica Sinica* **21**, 763–75 (in Chinese with English abstract).

Zhu Q, Zeng ZX, Li TB, Wang C and Liu GS (2018) Response of the North China Craton to the Rodinia supercontinent breakup: new evidence from petrochemistry, chronology and Hf isotope of the gabbro in Xiaosongshan area of northern Helan Mountain. *Geological Bulletin of China* **37**, 1075–86 (in Chinese with English abstract).

Zuo GC, Zhang SL, He GQ and Zhang Y (1990) Early Paleozoic tectonics in Beishan Area. *Chinese Journal of Geology* **4**, 305–14 (in Chinese).